AGU PUBLICATIONS

JGR

Journal of Geophysical Research: Earth Surface

RESEARCH ARTICLE

10.1002/2015JF003685

Key Points:
- Hydrodynamic analysis provides an insight into the physics of the flow in turbidity currents
- The velocity and concentration distributions show self-preserving characteristic
- Three-equation model is used to determine the characteristics of the parametric variables

Correspondence to:
F. N. Cantero-Chinchilla,
z12cachf@uco.es

Citation:
Cantero-Chinchilla, F. N., S. Dey, O. Castro-Orgaz, and S. Z. Ali (2015), Hydrodynamic analysis of fully developed turbidity currents over plane beds based on self-preserving velocity and concentration distributions, *J. Geophys. Res. Earth Surf.*, *120*, 2176–2199, doi:10.1002/2015JF003685.

Received 31 JUL 2015
Accepted 19 SEP 2015
Accepted article online 24 SEP 2015
Published online 27 OCTOBER 2015

Hydrodynamic analysis of fully developed turbidity currents over plane beds based on self-preserving velocity and concentration distributions

Francisco Nicolás Cantero-Chinchilla[1], Subhasish Dey[2], Oscar Castro-Orgaz[1], and Sk Zeeshan Ali[2]

[1]Department of Agronomy, University of Cordoba, Cordoba, Spain, [2]Department of Civil Engineering, Indian Institute of Technology Kharagpur, West Bengal, India

Abstract This paper presents a hydrodynamic analysis for the fully developed turbidity currents over a plane bed stemming from the classical three-equation model (depth-averaged fluid continuity, sediment continuity, and fluid momentum equations). The streamwise velocity and the concentration distributions preserve self-similarity characteristics and are expressed as single functions of vertical distance over the turbidity current layer. Using the experimental data of turbidity and salinity currents, the undetermined coefficients and exponents are approximated. The proposed relationships for velocity and concentration distributions exhibit self-preserving characteristics for turbidity currents. The depth-averaged velocity, momentum, and energy coefficients are thus obtained using the proposed expression for velocity law. Also, from the expressions for velocity and concentration, the turbulent diffusivity and the Reynolds shear stress distributions are deduced with the aid of the diffusion equation of sediment concentration and the Boussinesq hypothesis. The generalized equation of unsteady nonuniform turbidity current is developed by using the velocity and concentration distributions in the moments of the integral scales over the turbidity current layer. Then, the equation is applied to analyze the gradually varied turbidity currents considering closure relationships for boundary interaction and shear velocity. The streamwise variations of current depth, velocity, concentration, reduced sediment flux, and Richardson number are presented. Further, the self-accelerating and depositional characteristics of turbidity currents including the transitional feature from erosional to depositional modes are addressed. The effects of the streamwise bed slope are also accounted for in the mathematical derivations. The results obtained from the present model are compared with those from the classical model.

1. Introduction

Turbidity currents are gravity currents, which are often referred to as inclined plumes or underflows, consisting of a water-sediment mixture flowing over a sloping bed. In nature, high-density turbidity currents are able to carry such amount of suspended sediment that their erosive power usually produces remarkable geological reforms, e.g., submarine canyons [*Inman et al.*, 1976; *Fukushima et al.*, 1985; *Mastbergen and Van Den Berg*, 2003; *Sumner and Paull*, 2014]. Inland, man-made mining tailings, earthquakes, or heavy storms, among others can often originate turbidity currents with huge sediment mass, such as rocks or debris as underwater landslide to produce sediment-laden flows [*Normark and Dickson*, 1976; *Piper et al.*, 1999]. It is conceptually helpful to contemplate turbidity currents as a flow constituted by two separate parts, current head (that is the current front) and current body [*Stacey and Bowen*, 1988]. High suspended sediment concentration in turbidity currents produces a pressure gradient downslope arising from the density difference between the current head and the ambient water just in front of it and thus providing a driving force. The water-sediment mixture forming turbidity current, as a layer, is driven by the downslope gravitational component acting on the denser water-sediment mixture. Although it is in principle the same hydrodynamics as that driving the head, the buoyancy contrast between the turbidity current and the ambient water leads to a system where the downslope gradients of flow and sediment transport parameters may be small. The sediment-laden flow, however, generates adequate turbulence to hold the sediment particles in suspension. Uniform or gradually varied turbidity currents containing very fine sediments over a rigid bed were investigated by several investigators [*Bonnefille and Goddet*, 1959; *Stefan*, 1973; *Ashida and Egashira*, 1975].

Depending on the flow conditions, turbidity currents are distinguished as erosional or depositional underwater sediment-laden flows [*Akiyama and Stefan*, 1985]. The interaction of the turbidity current with the ambient flow can be envisaged as an entrainment of water from the ambient flow to the turbidity current

through the interface between them. In addition, in erodible beds, the sediment entrainment and deposition occur at the same time due to the interaction of the turbidity current with the bed layer. Under high erodible conditions, the sediment entrainment rate from the bed toward the turbidity current becomes sufficiently intense so that an inrushing of ambient water toward the turbidity current layer takes place to balance the mass and momentum fluxes. On the other hand, the entrainment of ambient water into the turbidity current gets reduced if sediment deposition occurs at the bed. In turn, the turbidity current becomes stagnant when there is no sediment transport. In other words, the thickness of the turbidity current layer is dependent on the ability of the flow to carry the suspended sediment particles. However, turbidity currents can be considered as self-generated currents in which sediment particles are suspended by the turbulence.

Less erosive gravity currents can be simulated in the laboratory environment by creating a salinity or temperature gradient. *Stacey and Bowen* [1988] stated that the competence of the flow to transport and suspend the sediment depends on the terminal fall velocity of sediment particles. In the limit, it is believed that for larger sediment particles, steady flow is not practically feasible. Salinity currents are good examples of containing sediments with a low terminal fall velocity. *Sequeiros et al*. [2010] conducted a large number of experiments on the velocity and the excess density distributions of saline and turbidity underflows. They observed the development of bed forms with time depending on the flow conditions. They also identified an upward shift of the reference level (that is, the demarcation level between bed and suspended load [*Dey*, 2014]) due to the change in bed roughness, as the bed forms grow with time. As a result, the velocity and concentration distributions are modified. *Nourmohammadi et al*. [2011] reported a study on the vertical distribution of gravity currents over a nonerodible bed. They observed a similarity in velocity and concentration distributions. Although the vertical distribution of velocity in turbidity currents seems not to be significantly affected by the suspended particle size [*Parker et al*., 1987; *Altinakar et al*., 1996], it is somehow interesting to analyze the effects of the terminal fall velocity on suspended sediment concentration.

In fact, the governing equations of turbidity current are similar to those used in sediment-laden flows. By applying the conservation laws of sediment-laden flows, the governing equations of turbidity current are obtained. *Akiyama and Stefan* [1985] introduced an analytical model based on the governing equations of turbidity current along with the entrainment and the depositional fluxes. The model, which was depth averaged into the one-dimensional form, constituted an extension of the formulation earlier reported by *Ellison and Turner* [1959]. Besides, the turbulent energy equation was accounted for reducing the formula to Bagnold's autosuspension concept [*Bagnold*, 1962]. However, their model was not verified due to nonavailability of the experimental data. *Parker et al*. [1986] presented a four-equation model, in which the mean turbulent kinetic energy (TKE) was considered. By considering the classical three-equation model (depth-averaged fluid continuity, sediment continuity, and fluid momentum equations [*Lai et al*., 2015]), as an extension from *Ellison and Turner* [1959] formulation, *Parker et al*. [1986] pointed out the importance of accurately predicting the bed sediment entrainment. *Stacey and Bowen* [1988] developed a simple numerical model (three equations) that matched well with the experimental data of velocity and concentration, although they initially failed to obtain the adequate solutions for the analytical model. Further, *Pratson et al*. [2000] solved the four-equation model developed by *Parker et al*. [1986] using numerical techniques. However, *Hu et al*. [2015] found that the three-equation model does not fail to simulate self-accelerating turbidity currents, rendering unclear the need of using the four-equation model. *Felix* [2001] proposed a two-dimensional turbulence model to address the development of turbidity current. In the same line, the large eddy simulation along with direct numerical simulation was also applied to simulate the turbidity currents [*Mahdinia et al*., 2011; *Dutta et al*., 2012]. On the other hand, as a new trend in simulation of gravity currents, the application of the thermal lattice Boltzmann method was also reported [*Lizhong et al*., 2011; *Prestininzi et al*., 2013]. However, in derivation of the full depth-averaged models, similarity solutions were sought for the convenience [*Parker et al*., 1986], assuming the velocity, concentration, and TKE distributions to preserve similarity.

Similarity approximation for the vertical distributions of the main flow characteristics are likely well justified in turbidity currents. Besides *Parker et al*. [1986] and *Stacey and Bowen* [1988], *Altinakar et al*. [1996] highlighted the self-similarity in velocity and concentration distributions. In this regard, *Stacey and Bowen* [1988] previously argued that the decoupling of the concentration from the temporal evolution of velocity is an inappropriate concept. Interestingly, their results suggested the self-preserving characteristic distributions for the flow characteristics. A turbidity current, as stated by *Altinakar et al*. [1996], can be viewed,

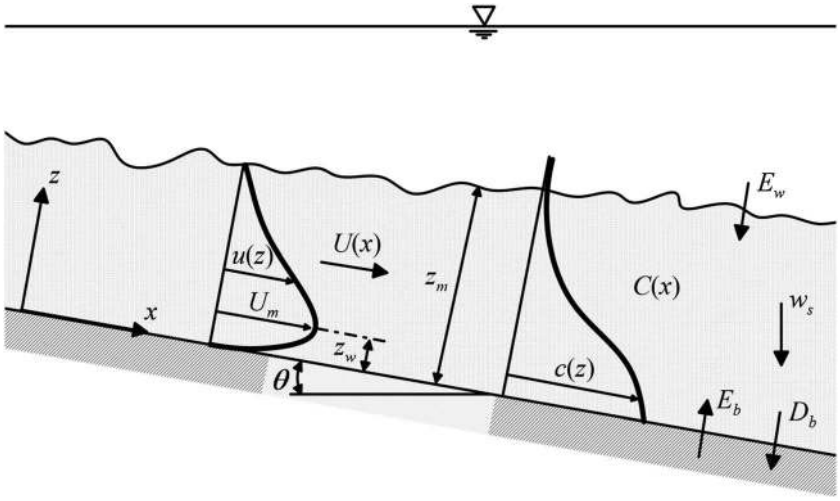

Figure 1. Definition sketch of a turbidity current on a sloping bed.

as far as the flow structure is concerned, analogous to a wall jet flow. Accordingly, *Altinakar et al*. [1996] assumed a power law for the velocity distribution and a linear law for the concentration distribution for the inner layer of flow (wall shear layer). For the outer layer of flow, they assumed the near-Gaussian relationships for the velocity and concentration distributions. These scaling laws gave a satisfactory agreement with their experimental data. It means that they considered different scaling laws for the inner and outer layers of flow. However, little attention has so far been paid to obtain the generalized scaling laws (represented by single functions) for the velocity and concentration distributions over the entire turbidity current layer. These generalized scaling laws, which should comply with the wide range of experimental data, are therefore a long due.

The objective of this study is to initially revisit the vertical distributions of velocity and concentration in turbidity currents to obtain single similarity functions (continuous over the entire layer) for them. Appropriate scaling for the similarity functions could bring the available experimental data of velocity and suspended sediment concentration for turbidity and salinity currents to single bands. This analysis thus provides us the self-preserving type relationships for the velocity and concentration distributions in turbidity currents. Using the developed similarity functions for the velocity and concentration, the Reynolds shear stress and turbulent diffusivity distributions are derived. Further, to enhance the mathematical model of the turbidity current according to the velocity and concentration distributions, three-equation model (depth-averaged fluid continuity, sediment continuity, and fluid momentum equations) is analyzed for gradually varied flow formulations using appropriate closure relationships.

2. Governing Equations

The problem of turbidity current is usually treated as a problem of incompressible turbulent flow [*Graf and Altinakar*, 1998]. When the fluid mass is sufficiently wide, the width has a minimal influence on the flow, and thus, the motion of the turbidity current can be approximated as a two-dimensional problem (x and z direction) (Figure 1) [*Parker et al*., 1986; *Akiyama and Stefan*, 1985]. Subsequently, the general depth-averaged equations of the fluid mass, sediment mass, and turbidity current momentum are as follows [*Parker et al*., 1986]:

$$\frac{\partial z_m}{\partial t} + \frac{\partial}{\partial x}\int_0^\infty u\,dz = -w_h, \tag{1}$$

$$\frac{\partial}{\partial t}\int_0^\infty c\,dz + \frac{\partial}{\partial x}\int_0^\infty uc\,dz = -w_s c|_b + \overline{c'w'}\Big|_b, \text{ and} \tag{2}$$

$$\frac{\partial}{\partial t}\int_0^\infty u\,dz + \frac{\partial}{\partial x}\int_0^\infty u^2\,dz = -\frac{1}{2}\Delta_s g\frac{\partial}{\partial x}\int_0^\infty\int_z^\infty c\,dz\,dz\cos\theta + \Delta_s g\int_0^\infty c\,dz\sin\theta - u_{*_b}^2, \tag{3}$$

where z_m is the vertical distance where velocity vanishes ($u=0$) into the turbidity current, considered to be the turbidity current depth, $u(z)$ is the streamwise velocity at a vertical distance z, w_h is the vertical velocity component at the top edge of the current, w_s is the terminal fall velocity of suspended sediment particles, $c(z)$ is the suspended sediment concentration at z, $\overline{c'w'}$ is the Reynolds flux of suspended particles, Δ_s is the submerged relative density [$=(\rho_s-\rho_a)/\rho_a$], ρ_s is the mass density of sediment particles, ρ_a is the mass density of ambient fluid, g is the gravitational acceleration, θ is the streamwise bed slope, u_{*b} is the shear velocity, and subscript b refers to bed. In Figure 1, the depth-averaged sediment concentration in turbidity current is given by $C(x)$. It may be noted that in four-equation model [*Parker et al*., 1986], the TKE budget is included as the fourth equation, which is briefly discussed in Appendix A.

In equations (1)–(3), the boundary layer approximations for a two-dimensional turbidity current are considered. Henceforth, the turbidity current is considered as a fully turbulent flow. Thereby, only the viscous dissipation due to turbulence remains, neglecting other viscous terms. Also, the vertical flux terms appearing in the right-hand side of the equation (2) are evaluated somewhat above the lower boundary to avoid singular solutions related to the vanishing molecular diffusivity. Equation (3) accounts for the nonhydrostatic treatment of turbidity currents, decomposing the actual pressure into a component due to the ambient fluid and an additional component due to the presence of sediment particles. Thus, the terms in the right-hand side of equation (3) are regarded as the pressure force of the turbidity current.

The integrals in equations (1)–(3), which define the depth-averaged quantities of the flow, are known as the moments of the integral scales [*Ellison and Turner*, 1959; *Turner*, 1973]. They are

$$I_1=\int_0^\infty u\mathrm{d}z, I_2=\int_0^\infty u^2\mathrm{d}z, \quad \text{and} \tag{4}$$

$$I_3=\int_0^\infty c\mathrm{d}z,\ \ I_4=\int_0^\infty uc\mathrm{d}z,\ \ I_5=\int_0^\infty\int_z^\infty c\mathrm{d}z\mathrm{d}z. \tag{5}$$

Equations (1)–(3) can be expressed by means of interaction processes that occur at the interface of the layers (turbidity current and ambient fluid layers). The static pressure in the ambient still fluid is greater than the actual pressure in the turbidity current. According to the Bernoulli equation, a negative pressure gradient in the upper layer (ambient fluid layer) results in an inward movement of ambient fluid into the turbidity current through the interface. Therefore, the entrainment velocity is assumed to be proportional to the velocity of the turbidity current [*Turner*, 1973], $-w_h=E_wU$, where E_w is the entrainment coefficient of ambient fluid and $U(x)$ is the depth-averaged velocity of the turbidity current. Besides, according to *Parker et al*. [1987], the first and second terms in the right-hand side of equation (2) can be identified as the erosion rate E_b and deposition D_b rate of sediment at the bed (Figure 1). Therefore,

$$w_sc|_b=D_b \quad \text{and} \tag{6}$$

$$\overline{c'w'}\Big|_b=E_b. \tag{7}$$

Thus, the three-equation model is finally written as follows:

$$\frac{\partial z_m}{\partial t}+\frac{\partial I_1}{\partial x}=E_wU, \tag{8}$$

$$\frac{\partial I_3}{\partial t}+\frac{\partial I_4}{\partial x}=E_b-D_b, \quad \text{and} \tag{9}$$

$$\frac{\partial I_1}{\partial t}+\frac{\partial I_2}{\partial x}=-\frac{1}{2}\Delta_sg\frac{\partial I_5}{\partial x}\cos\theta+\Delta_sgI_3\sin\theta-u_{*b}^2. \tag{10}$$

The streamwise bed slope $\sin\theta$ cannot be ignored, since a turbidity current is, by nature, a sloping flow inside a greater mass of fluid [*Graf and Altinakar*, 1998], as shown in Figure 1. Accordingly, $\cos\theta$ cannot be simplified as unity.

Note that following *Graf* [1971] and *Parker et al*. [1986], the erosion and deposition rates E_b and D_b appear in the mass conservation for the suspended sediment phase, equation (9), whereas the mass conservation equation for the water phase is free from exchange terms. These terms appear as well in the mixture mass conservation equation of a turbidity current [*Hu et al*., 2012].

3. Velocity Distribution

In a fully developed state, the velocity distribution in turbidity current is almost similar to that in submerged plane wall jet. A submerged plane wall jet is described as a jet of fluid that impinges tangentially (or at an angle) on a solid wall surrounded by the same fluid (stationary or moving) progressing along the wall [*Dey et al*., 2010]. For a turbidity current, on one side (in the inner layer), the current is confined to the bed, while on the other side (in the outer layer), it is bounded by the stationary ambient fluid (Figure 1). The boundary conditions for the velocity distribution in turbidity current are such that the velocity vanishes at the bed and at the interface between the turbidity current and the ambient fluid. Thus, the velocity distribution attains a maximum (peak velocity) at the extremity of the inner layer, that is, the junction of the inner and outer layers of the current. Below the maximum velocity level (in the inner layer), the flow is featured by a boundary layer flow, while above the maximum velocity level (in the outer layer), the flow is structurally similar to a free jet. Therefore, the turbidity currents are characterized by an inner shear layer influenced by the bed and an outer layer of the self-similar type of a shear flow [*Parker et al*., 1987; *Stacey and Bowen*, 1988; *Altinakar et al*., 1996; *Shringarpure et al*., 2012]. For the similarity in velocity distributions, the nondimensional variables introduced are $\hat{u} = u/U_m$ and $\eta = z/z_m$, where U_m is the maximum velocity. Previous studies primarily assumed two separate velocity distributions for the inner and outer layers of turbidity currents. However, in this study, a single velocity distribution over the entire range of the inner and outer layers is assumed in the following form:

$$\hat{u}(\eta) = \sigma \eta^{\xi} (1-\eta)^{\chi}, \tag{11}$$

where σ is a coefficient and ξ and χ are the exponents. They are the unknown parameters to be determined from the experimental data. It is pertinent to mention that the nondimensional velocity distribution in equation (11) is considered as a combination of a power function η^{ξ} and a wake function $(1-\eta)^{\chi}$ in order to preserve the boundary conditions, namely, $\hat{u}(\eta = 0) = 0$ and $\hat{u}(\eta = 1) = 0$. Besides, the product of those functions in equation (11) corresponds to the study of *Islam and Imran* [2010]. Equation (11) shows that the velocity distribution in the inner layer is analogous to a boundary layer flow, while that in the outer layer is similar to a free jet. The maximum velocity U_m occurs at a location $z = z_w$. Introducing $\eta_w = z_w/z_m$ at the occurrence of the maximum velocity, another boundary condition $\hat{u}(\eta = \eta_w) = 1$ is satisfied at the extremity of the inner layer. Therefore, from equation (11), one obtains

$$\sigma = \eta_w^{-\xi} (1-\eta_w)^{-\chi}. \tag{12}$$

The velocity gradient at $z = z_w$ vanishes due to the occurrence of maximum velocity at that level, that is $\mathrm{d}\hat{u}/\mathrm{d}\eta\ (\eta = \eta_w) = 0$. Applying this boundary condition, equation (11) produces

$$\eta_w = \frac{\xi}{\xi + \chi}. \tag{13}$$

Substituting equation (13) into equation (12) yields

$$\sigma = \frac{(\xi + \chi)^{\xi + \chi}}{\xi^{\xi} \chi^{\chi}}. \tag{14}$$

Equation (14) shows the dependency of the coefficient σ on the exponents ξ and χ. The exponents ξ and χ are to be determined using the experimental data.

Figure 2 displays the computed velocity distributions obtained from equation (11) and using two equations given by *Altinakar et al*. [1996]. The experimental data plots of turbidity and salinity currents obtained from

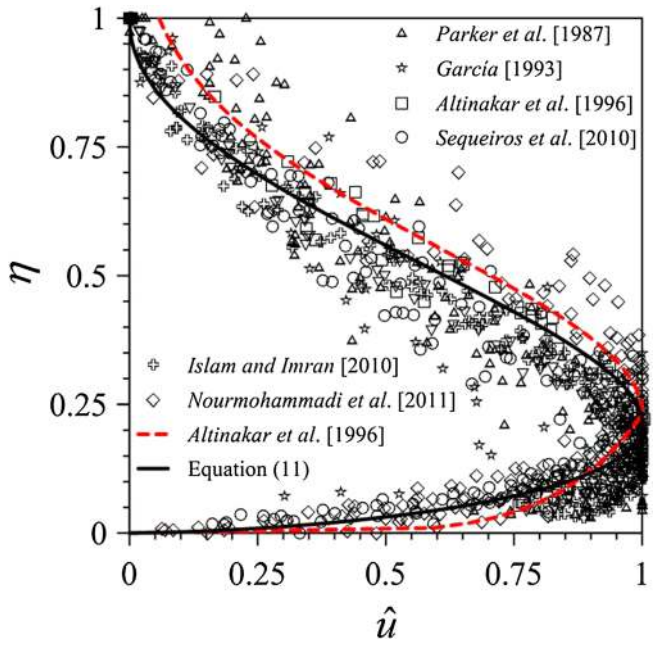

Figure 2. Computed velocity distribution $\hat{u}(\eta)$ obtained from equation (11) showing the comparison with the velocity distribution obtained using two equations given by *Altinakar et al.* [1996] and the experimental data of different investigations.

Parker et al. [1987], *García* [1993], *Altinakar et al.* [1996], *Sequeiros et al.* [2010], *Islam and Imran* [2010], and *Nourmohammadi et al.* [2011] are overlapped on the computed curves in Figure 2 for comparison. It is found that the values $\xi = 0.6$ and $\chi = 2.2$ ensure a satisfactory agreement of equation (11) with the experimental data. Therefore, from equation (14), one obtains $\sigma = 4.28$. The standard deviation, standard error, and correlation coefficient for Figure 2 are 0.333, 0.011, and 0.930, respectively, which provide a quantitative understanding on the data scatter from equation (11). The occurrence of the maximum velocity determined from equation (13) is $\eta_w = 0.214$. In Figure 2, the experimental data of runs 6–10, 12, 13, 17, 20, 23, and 24 from *Parker et al.* [1987] are shown. From *García* [1993], run DAPER6 is also selected for the peak velocity data in subcritical and supercritical flow conditions. Three sets of experimental data are taken from *Altinakar et al.* [1996]. Among them, two sets belong to the turbidity currents with sediment sizes $d = 0.047$ and 0.026 mm, where d is the median size of sediment particles, and the third set belongs to the salinity current. From *Sequeiros et al.* [2010], the experimental data for runs 2, 10, 16, 23, 31, 36–38, 40, and 41, in which no bed forms occurred, are considered. The experimental velocity data of sections 1–12 for salinity and turbidity currents reported by *Islam and Imran* [2010] are extracted. Besides, from *Nourmohammadi et al.* [2011], the experimental data for run 3 at streamwise distances of 2.5 and 3.5 m, run 10 at 4.5 m, and runs 7 and 8 at 3.5 and 4.5 m, respectively, from the flume inlet are used. Finally, the computed velocity distribution of *Altinakar et al.* [1996] over predicts most of the experimental data (Figure 2).

From Figure 2, it is observed that the following empirical relationship between ξ and χ shows a good agreement between the fitted velocity distribution and the experimental data:

$$\chi \approx 1 + 2\xi. \tag{15}$$

Therefore, using equations (14) and (15), equation (11) takes the following form:

$$\hat{u} = \frac{(1+3\xi)^{1+3\xi}}{\xi^{\xi}(1+2\xi)^{1+2\xi}}\,\eta^{\xi}(1-\eta)^{1+2\xi}. \tag{16}$$

Equation (16) thus provides the velocity distribution in turbidity currents with a single free parameter ξ, which was empirically determined as 0.6. This relationship for the velocity distribution is in fact of self-preserving type for turbidity currents.

The depth-averaged velocity U in nondimensional form is

$$\hat{U} = \int_0^1 \hat{u}\,\mathrm{d}\eta, \tag{17}$$

where $\hat{U} = U/U_m$. Inserting equation (16) into equation (17) yields

$$\hat{U} = \frac{(1+3\xi)^{1+3\xi}}{\xi^{\xi}(1+2\xi)^{1+3\xi}} \cdot \frac{\Gamma(1+\xi)\Gamma(2+2\xi)}{\Gamma(3+3\xi)}, \tag{18}$$

where $\Gamma(s)$ is the Euler gamma function defined as

$$\Gamma(s) = \int_0^{\infty} y^{s-1}\exp(-y)\mathrm{d}y. \tag{19}$$

Since the velocity distribution is obtained from equation (16), typically the flow parameters of interest, such as momentum (Boussinesq) coefficient, energy (Coriolis) coefficient, and the moments of the integral scales defined in equation (4), are determined.

The momentum (Boussinesq) coefficient β is defined as

$$\beta = \frac{\int_0^{z_m} u^2\mathrm{d}z}{U^2 z_m} = \frac{\int_0^1 \hat{u}^2\mathrm{d}\eta}{\hat{U}^2}. \tag{20}$$

Inserting equations (16) and (18) into equation (20) yields

$$\beta = \frac{1}{\hat{U}^2} \cdot \frac{(1+3\xi)^{2+6\xi}}{\xi^{2\xi}(1+2\xi)^{2+4\xi}} \cdot \frac{\Gamma(1+2\xi)\Gamma(3+4\xi)}{\Gamma(4+6\xi)}. \tag{21}$$

The energy (Coriolis) coefficient α is defined as

$$\alpha = \frac{\int_0^{z_m} u^3\mathrm{d}z}{U^3 z_m} = \frac{\int_0^1 \hat{u}^3\mathrm{d}\eta}{\hat{U}^3}. \tag{22}$$

Inserting equations (16) and (18) into equation (22) yields

$$\alpha = \frac{1}{\hat{U}^3} \cdot \frac{(1+3\xi)^{3+9\xi}}{\xi^{3\xi}(1+2\xi)^{3+6\xi}} \cdot \frac{\Gamma(1+3\xi)\Gamma(4+6\xi)}{\Gamma(5+9\xi)}. \tag{23}$$

With $\xi = 0.6$, the following parameters are obtained from equations (18), (21), and (23):

$$\hat{U} = 0.52,\ \beta = 1.465,\ \alpha = 2.366. \tag{24}$$

The moments of the integral scales in equation (4) are determined as

$$I_1 = \int_0^{\infty} u\mathrm{d}z = \int_0^{z_m} u\mathrm{d}z = 0.52U_m z_m \quad \text{and} \tag{25}$$

$$I_2 = \int_0^{\infty} u^2\mathrm{d}z = \int_0^{z_m} u^2\mathrm{d}z = 0.396U_m^2 z_m. \tag{26}$$

For details of integral equations (25) and (26), see Appendix B.

4. Concentration Distribution

In accordance with the mechanism of suspended sediment motion, the turbidity current can be considered as a self-generated current in which sediment particles are suspended by the turbulence. The transport of suspended sediment particles in turbulent flow takes place due to the advection and diffusion processes in the ambient fluid. The governing equation of the diffusion of suspended sediment concentration shows a remarkable dependency of the concentration distribution on the velocity distribution [*Dey*, 2014]. The concentration distribution in turbidity current is therefore affected by the velocity distribution, allowing two distinctive zones. Above the maximum velocity level ($z > z_w$), the concentration distribution asymptotically vanishes ($c \to 0$) just above z_m, and beneath the maximum velocity level ($z \leq z_w$), the concentration distribution follows a classical boundary layer approximation. For the similarity in concentration distributions, the nondimensional variable is introduced as $\hat{c} = c/C_m$, where C_m is the concentration at $\eta = \eta_w$.

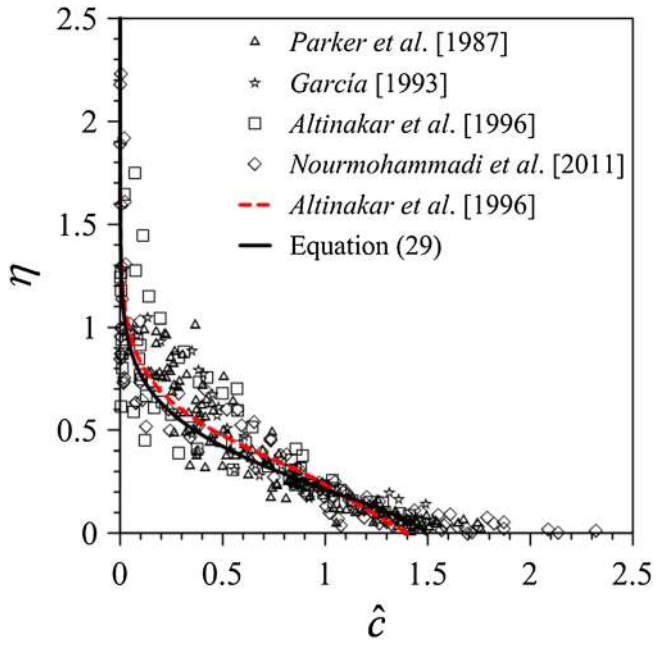

Figure 3. Computed concentration distribution $\hat{c}(\eta)$ obtained from equation (29) showing the comparison with the concentration distribution obtained using two equations given by *Altinakar et al.* [1996] and the experimental data of different investigations.

Unlike the previous studies which considered two separate expressions for concentration distributions in the inner and outer layers of turbidity currents [*Altinakar et al.*, 1996], a single concentration distribution over the entire range of the inner and outer layers is assumed here in the following form:

$$\hat{c}(\eta) = \lambda \exp\left(-\phi\eta^{\zeta}\right), \tag{27}$$

where λ, ϕ, and ζ are the unknown parameters. Equation (27) shows that the concentration has a decreasing trend with the vertical distance. It also provides a finite value of concentration c_0 at the bed ($\eta = 0$). Importantly, equation (27) does not consider any reference level for the concentration distribution in particular. Applying the boundary condition, $\hat{c}(\eta = \eta_w) = 1$ to equation (27) yields

$$\lambda = \exp\left(\phi\eta_w^{\zeta}\right). \tag{28}$$

Substituting equation (28) into equation (27) yields

$$\hat{c}(\eta) = \exp\left[-\phi\left(\eta^{\zeta} - \eta_w^{\zeta}\right)\right]. \tag{29}$$

Figure 3 presents the computed concentration distributions obtained from equation (29) and using two equations proposed by *Altinakar et al.* [1996]. The experimental data of *Parker et al.* [1987], *García* [1993], *Altinakar et al.* [1996], and *Nourmohammadi et al.* [2011] for gravity currents are shown in Figure 3 for comparison. In addition, the values $\phi = 4$ and $\zeta = 1.5$ provide a best fitting of the computed curve with the experimental data. Therefore, with $\eta_w = 0.214$ in equation (28), the λ is obtained as 1.486. The standard deviation, standard error, and coefficient of correlation in Figure 3 are 0.526, 0.029, and 0.949, respectively, which provide an insight of the data scatter from equation (29). In Figure 3, the experimental data for runs 6–10, 12, 13, 17, 20, 23, and 24 from *Parker et al.* [1987] and runs DAPER6 in subcritical and supercritical conditions from *García* [1993] are shown. From *Altinakar et al.* [1996], three sets of experimental data used in the velocity distributions as mentioned before are considered for the concentration distribution, whereas from *Nourmohammadi et al.* [2011], the experimental data for runs 5 and 6 at 2.5 and 5.5 m, respectively, and run 3 at 2.5 and 3.5 m from the flume inlet are considered. Finally, the computed concentration distribution of *Altinakar et al.* [1996] corresponds to the curve obtained from the present study (Figure 3).

From the data plots in Figure 3, an empirical relationship between the parameters ϕ and ζ are obtained as

$$\phi = 5\zeta - 3.5. \tag{30}$$

Substituting equation (30) into equation (29), the concentration distribution is

$$\hat{c}(\eta) = \exp\left[-(5\zeta - 3.5)\left(\eta^{\zeta} - \eta_w^{\zeta}\right)\right]. \tag{31}$$

This relationship for the concentration distribution is indeed self-preserving type for turbidity currents.

From equation (31), the sediment concentration c_0 at the bed ($\eta = 0$) in nondimensional form is

$$\hat{c}_0 = \exp\left[(5\zeta - 3.5)\eta_w^{\zeta}\right], \tag{32}$$

where $\hat{c}_0 = c_0/C_m$. The depth-averaged concentration C in nondimensional form is

$$\hat{C} = \int_0^1 \hat{c}\,\mathrm{d}\eta, \tag{33}$$

where $\hat{C} = C/C_m$. Inserting equation (31) into equation (33) yields

$$\hat{C} = \frac{1}{\zeta}(5\zeta - 3.5)^{-1/\zeta}\exp\left[5(\zeta - 0.7)\eta_w^{\zeta}\right]\left[\Gamma\left(\frac{1}{\zeta}\right) - \Gamma\left(\frac{1}{\zeta},\ 5\zeta - 3.5\right)\right], \tag{34}$$

where $\Gamma(a, s)$ is the incomplete gamma function defined as

$$\Gamma(a, s) = \int_s^{\infty} y^{a-1}\exp(-y)\mathrm{d}y. \tag{35}$$

For $\zeta = 1.5$ and $\eta_w = 0.214$, equation (34) yields $\hat{C} = 0.528$.

Equation (31) suggests that the concentration distribution has a finite value at $z = z_m\,(\eta = 1)$, although it is feeble. For $\eta > 1$, the asymptotic trend of $\hat{c}(\eta)$ toward the ordinate is evident (Figure 3). The area under the curve $\hat{c}(\eta)$ bounded by $\eta = 0$ and $\hat{c} = 0$ for the two cases when the limits of integration are $\eta = 0$ to 1 and $\eta = 0$ to 2.5 shows an approximate relative error of 0.7%. Thus, the upper limit of the moments of the integral scales defined in equation (5) is considered at $z = z_m\,(\eta = 1)$. Hence, the integral scales in equation (5) are given by

$$I_3 = \int_0^{\infty} c\mathrm{d}z = \int_0^{z_m} c\mathrm{d}z = 0.528\,C_m z_m, \tag{36}$$

$$I_4 = \int_0^{\infty} uc\mathrm{d}z = \int_0^{z_m} uc\mathrm{d}z = 0.396\,U_m C_m z_m, \quad \text{and} \tag{37}$$

$$I_5 = \int_0^{\infty}\int_z^{\infty} c\mathrm{d}z\mathrm{d}z = \int_0^{z_m}\int_z^{z_m} c\mathrm{d}z\mathrm{d}z = 0.743\,C_m z_m^2. \tag{38}$$

For details of the moments of the integral equations (36)–(38), see Appendix B.

5. Reynolds Shear Stress and Turbulent Diffusivity Distributions

In a fully developed turbulent flow, the Reynolds shear stress is much greater than the viscous shear stress except in the vicinity of the bed, where the flow is laminar within a thin viscous sublayer. It may be noted that the Reynolds shear stress nearly composes the total shear stress (Reynolds shear stress and viscous shear stress) in the absence of viscous shear stress. Since the turbidity current is characterized by the turbulent flow, the molecular diffusivity is negligible as compared to the turbulent diffusivity. Moreover, the solid diffusivity is considered approximately equalling the turbulent diffusivity [*Rouse*, 1937; *Dey*, 2014]. Hence, the Reynolds shear stress and the turbulent diffusivity distributions are determined from the proposed velocity and concentration distributions (equations (16) and (31)).

The suspended sediment stratification due to turbidity affects the structure of the turbulent diffusivity in turbidity currents [*Stacey and Bowen*, 1988]. From the diffusion equation of suspended sediment concentration, the turbulent diffusivity ε_t is defined as

$$\varepsilon_t = -w_s c\left(\frac{\mathrm{d}c}{\mathrm{d}z}\right)^{-1}. \tag{39}$$

The nondimensional turbulent diffusivity $\hat{\varepsilon}_t$ is then expressed as

$$\hat{\varepsilon}_t = -Z\hat{c}\left(\frac{\mathrm{d}\hat{c}}{\mathrm{d}\eta}\right)^{-1}, \tag{40}$$

where $\hat{\varepsilon}_t = \varepsilon_t/(\kappa u_{*b} z_m)$, κ is the von Kármán constant, and Z is the Rouse number $[= w_s/(\kappa u_{*b})]$. Using equation (31), equation (40) reduces to

$$\hat{\varepsilon}_t = Z\frac{\eta^{1-\zeta}}{(5\zeta - 3.5)\zeta}. \tag{41}$$

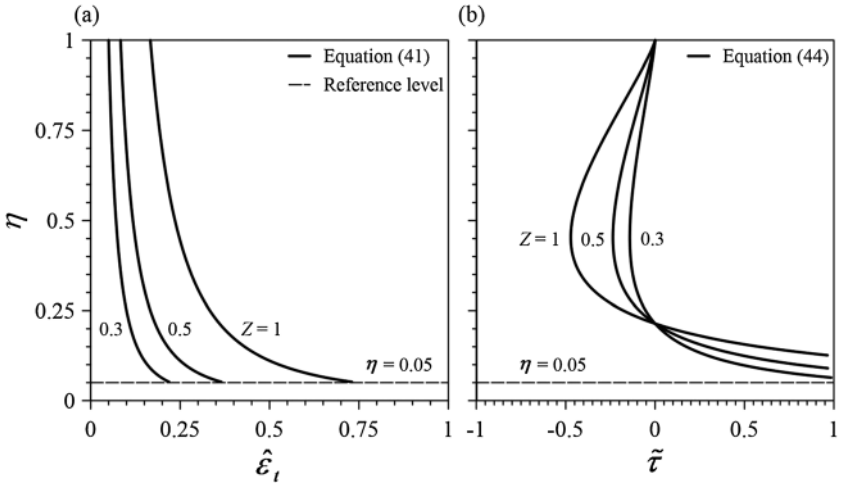

Figure 4. Distributions of computed turbulent diffusivity $\hat{\varepsilon}_t(\eta)$ and Reynolds shear stress $\tilde{\tau}(\eta)$ for different Rouse numbers Z(= 0.3, 0.5, and 1) obtained from the present model.

According to the Boussinesq hypothesis, the Reynolds shear stress τ in turbulent flow is expressed as

$$\tau = \rho \varepsilon_t \frac{du}{dz}, \tag{42}$$

where ρ is the mass density of the fluid-sediment mixture. In nondimensional form, the Reynolds shear stress is

$$\hat{\tau} = \hat{\varepsilon}_t \frac{U_m}{u_{*_b}} \cdot \frac{d\hat{u}}{d\eta}, \tag{43}$$

where $\hat{\tau} = \tau/(\rho\, u_{*_b}^2)$. Substituting equations (16) and (41) into equation (43) yields

$$\tilde{\tau} = Z \frac{\eta^{1-\zeta}}{(5\zeta - 3.5)\zeta} (1-\eta)^{2\xi} \eta^{-1+\xi} \xi^{-\xi} (1+2\xi)^{-1-2\xi} (1+3\zeta)^{1+3\xi} [\xi - \eta(1+3\xi)], \tag{44}$$

where $\tilde{\tau} = \hat{\tau}\,(u_{*b}/U_m)$.

The turbulent diffusivity and the Reynolds shear stress are computed from equations (41) and (44), respectively, using $\xi = 0.6$ and $\zeta = 1.5$. Figures 4a and 4b show the variations of computed nondimensional turbulent diffusivity $\hat{\varepsilon}_t$ and Reynolds shear stress $\tilde{\tau}$ with nondimensional vertical distance η for Rouse numbers $Z = 0.3$, 0.5, and 1. The nondimensional reference level considered at $\eta = 0.05$, according to *Graf and Altinakar* [1998], is also shown.

At the reference level ($\eta = 0.05$), the $\hat{\varepsilon}_t$ is maximum. Then, the $\hat{\varepsilon}_t$ decreases with an increase in η approaching a constant value for $\eta > 1$. It implies that $\hat{\varepsilon}_t$ has a finite value at the upper boundary of the turbidity current ($\eta = 1$). This feature can be explained from the viewpoint of the applicability of the governing equation of suspended sediment concentration (equation (39)). Strictly, equation (39) is only applicable to steady uniform flows. However, as an approximation, the present study assumes that equation (39) is applicable to nonuniform flows. On the other hand, the entrainment of ambient fluid into the turbidity current induces a significant mixing at the interface between the turbidity current and the ambient fluid. Hence, a finite value of $\hat{\varepsilon}_t$ at the upper boundary of the turbidity current is meaningful. Another important feature is that for a given η, $\hat{\varepsilon}_t$ increases with an increase in Z.

In case of Reynolds shear stress, in the immediate vicinity above the reference level ($\eta = 0.05$), the $\tilde{\tau}$ is positive. It diminishes with an increase in η within the inner layer following a similar trend of $\tilde{\tau}$ distribution in a boundary layer flow due to the reduction in velocity gradient with η and becomes zero at the point of occurrence of maximum velocity. With a further increase in η (within the outer layer), the $\tilde{\tau}$ becomes negative forming a protuberance (maximum negative value of $\tilde{\tau}$ in $\tilde{\tau}$ distribution) at the point of inflection of the $\hat{u}$ distribution, and then it gradually approaches to zero. It is relevant to mention that a similar trend of $\tilde{\tau}$ distribution was observed by *Dey et al.* [2010] in a submerged wall jet. For a given η, $\tilde{\tau}$ decreases with an increase in Z in the outer layer, while in the inner layer, $\tilde{\tau}$ increases with Z.

6. Turbidity Current Model and Gradually Varied Flow Formulations

Since velocity and the concentration distributions are known, the three-equation model for the turbidity currents is obtained by inserting $\hat{U}=0.52$, $\beta=1.465$, $\alpha=2.366$, and the moments of the integral scales of equations (25), (26), (36)–(38) into equations (8)–(10). Therefore, the three-equation model is

$$\frac{\partial z_m}{\partial t}+0.52\frac{\partial(U_m z_m)}{\partial x}=0.52E_w U_m, \tag{45}$$

$$0.528\frac{\partial(C_m z_m)}{\partial t}+0.396\frac{\partial(U_m C_m z_m)}{\partial x}=E_b-D_b, \quad \text{and} \tag{46}$$

$$0.52\frac{\partial(U_m z_m)}{\partial t}+0.396\frac{\partial\left(U_m^2 z_m\right)}{\partial x}=-0.372\Delta_s g\frac{\partial\left(C_m z_m^2\right)}{\partial x}\cos\theta+0.528\Delta_s g C_m z_m\sin\theta-u_{*_b}^2. \tag{47}$$

For a steady flow, time derivatives in equations (45)–(47) disappear. Therefore, using equations (45)–(47) under the steady flow condition yields the gradually varied flow formulations for z_m and C_m as

$$\frac{\mathrm{d}z_m}{\mathrm{d}x}=\frac{1}{1-0.961\mathrm{Ri}}\left[1.213\mathrm{Ri}\frac{E_b-D_b}{U_m C_m}+\frac{1}{2}(4-0.961\mathrm{Ri})E_w-0.683\mathrm{Ri}\tan\theta+2.525\left(\frac{u_{*_b}}{U_m}\right)^2\right], \tag{48}$$

$$\frac{\mathrm{d}C_m}{\mathrm{d}x}=\frac{1}{U_m z_m}\left(\frac{E_b-D_b}{0.396}-E_w U_m C_m\right), \tag{49}$$

where Ri is the Richardson number given by

$$\mathrm{Ri}=\frac{\Delta_s g C z_m\cos\theta}{U^2}=1.952\frac{\Delta_s g C_m z_m\cos\theta}{U_m^2}. \tag{50}$$

The streamwise variation of Ri is obtained as

$$\frac{\mathrm{dRi}}{\mathrm{d}x}=\frac{3\mathrm{Ri}}{z_m(1-0.961\mathrm{Ri})}\left[\frac{1}{2}(2+0.961\mathrm{Ri})\left(E_w+\frac{1}{3}\cdot\frac{E_b-D_b}{0.396U_m C_m}\right)-0.683\mathrm{Ri}\tan\theta+2.525\left(\frac{u_{*_b}}{U_m}\right)^2\right]. \tag{51}$$

Further, Ri is expressed in terms of the reduced sediment flux B as

$$\mathrm{Ri}=1.952\frac{\Delta_s g C_m z_m U_m\cos\theta}{U_m^3}=7.098\frac{B\cos\theta}{U_m^3}, \tag{52}$$

where $B=\Delta_s g C U z_m=0.275\Delta_s g C_m U_m z_m$. The B can be interpreted as the sediment transport rate CUz_m affected by the gravitational acceleration reduced by the buoyancy effect $\Delta_s g$ [*Graf and Altinakar*, 1998; *Wang et al.*, 2010]. Differentiating equation (52), the streamwise gradient of B is expressed as

$$\frac{\mathrm{d}B}{\mathrm{d}x}=\frac{U_m^3}{7.098\cos\theta}\cdot\frac{\mathrm{dRi}}{\mathrm{d}x}+3\frac{B}{z_m}\left(E_w-\frac{\mathrm{d}z_m}{\mathrm{d}x}\right). \tag{53}$$

Substituting equations (48) and (51) into equation (53) yields

$$\frac{\mathrm{d}B}{\mathrm{d}x}=\frac{B}{z_m}\cdot\frac{E_b-D_b}{0.396U_m C_m}. \tag{54}$$

7. Closure Relationships

Closure relations are required to evaluate the boundary interaction functions and the bed shear stress involved in the formulations in the preceding sections. The parameters involved with them are often specified by empirical relationships reported in literature.

The empirical relationship for the entrainment coefficient of ambient fluid E_w was proposed by *Parker et al.* [1987] and was extended to gravity currents by *Altinakar et al.* [1993] using the experimental data of turbidity currents and density currents [*Graf and Altinakar*, 1998]. It is

$$E_w=0.075\left(1+718\mathrm{Ri}^{2.4}\right)^{-0.5}. \tag{55}$$

The net sediment rate ($E_b - D_b$) is then expressed as

$$E_b - D_b = w_s(E_s - c_b), \tag{56}$$

where E_s is the entrainment coefficient of sediment particles from the bed and c_b is the reference suspended sediment concentration. The empirical relationship for E_s given by *Parker et al*. [1987], which was used by *Altinakar et al*. [1996] and *Graf and Altinakar* [1998], is considered here. It is

$$E_s = 3\times10^{-11}\left(\frac{u*_b}{w_s}\mathrm{Re}_p^{0.75}\right)^7\left[1+10^{-10}\left(\frac{u*_b}{w_s}\mathrm{Re}_p^{0.75}\right)^7\right]^{-1}, \tag{57}$$

where Re_p is the particle Reynolds number [$=(\Delta_s g d^3/\upsilon^2)^{0.5}$] and υ is the kinematic viscosity of fluid.

The c_b is usually evaluated in the vicinity of the bed at $\eta = 0.05$ as indicated in Figure 4. According to *Graf* [1971], c_b is expressed as

$$\frac{c_b}{C} = f\left(\frac{u*_b}{w_s}\right). \tag{58}$$

From the experimental observation concerning turbidity currents, it was found that $c_b/C \approx 2$ for $1 < u*_b/w_s < 50$. [*Parker et al*., 1987; *Altinakar et al*., 1993], However, this relationship can be revised and extended to salinity currents as well using the concentration distribution proposed in this study. Evaluating equation (31) at the nondimensional reference level ($\eta = 0.05$), equation (58) is expressed as

$$\frac{c_b}{C_m} = 1.421,\ \frac{c_b}{C} = 2.691. \tag{59}$$

Equations (56) and (57) show the dependency of ($E_b - D_b$) and E_s on terminal fall velocity w_s. Hence, the determination of w_s for a given sediment size is an essential prerequisite. For natural sediment particles, different formulas are available to evaluate w_s in turbid fluid [*Hallermeier*, 1981; *Chang and Liou*, 2001; *Guo*, 2002] and still fluid [*Dietrich*, 1982; *Ahrens*, 2000; *Wu and Wang*, 2006]. A summary of the formulas of w_s is available in *Dey* [2014]. *Zhang and Xie*'s [1993] empirical formula, which agreed well with the experimental data over a wide range of sediment sizes from laminar to turbulent flow [*Wu*, 2008], is considered here. It is

$$w_s = \left[1.09\Delta_s g d + \left(\frac{13.95\upsilon}{d}\right)^2\right]^{0.5} - \frac{13.95\upsilon}{d}. \tag{60}$$

The $u*_b$ is determined as follows:

$$u*_b = U\left(\frac{\lambda_D}{8}\right)^{0.5} = 0.52U_m\left(\frac{\lambda_D}{8}\right)^{0.5}, \tag{61}$$

where λ_D is the Darcy-Weisbach friction factor.

8. Numerical Experiment

A numerical example is selected from *Graf and Altinakar*'s [1998, 7.7.1, p. 491] book, where the initial values of $z_{m0} = 1$ m, $U_0 = 1$ m s^{-1}, and $C_0 = 0.0212$ are considered for the computation. The initial reduced sediment flux B_0 is calculated from $B_0 = 0.275\Delta_s g C_0 U_0 z_0$. The streamwise bed slope $\theta = 5°$, mass density of sediment particles $\rho_s = 2650$ kg m^{-3}, mass density of water $\rho_a = 1000$ kg m^{-3}, and friction factor $\lambda_D = 0.032$ are assumed. The total length of the channel reach is taken as 4000 m. The gradually varied flow formulations (equations (48), (49), (51), and (54)) derived in section 6 are solved numerically using the fourth-order Runge-Kutta method along with a first-order forward difference scheme. The numerical scheme is proved to be independent of the grid size. Here $\Delta\hat{x}$ ($=\Delta x/z_{m0}$) is considered as 0.5 to ensure a smooth variation of parametric variables. The parametric variables for turbidity currents are specified as

$$\widetilde{z}_m = \frac{z_m}{z_{m0}},\ \widetilde{U} = \frac{U}{U_0},\ \widetilde{C} = \frac{C}{C_0},\ \widetilde{\mathrm{Ri}} = \frac{\mathrm{Ri}}{\mathrm{Ri}_0},\ \widetilde{B} = \frac{B}{B_0}, \tag{62}$$

where z_m is the nondimensional turbidity current depth, $\widetilde{U}$ is the nondimensional depth-averaged velocity, $\widetilde{C}$ is the nondimensional depth-averaged concentration, $\widetilde{\mathrm{Ri}}$ is the relative Richardson number, and $\widetilde{B}$ is the

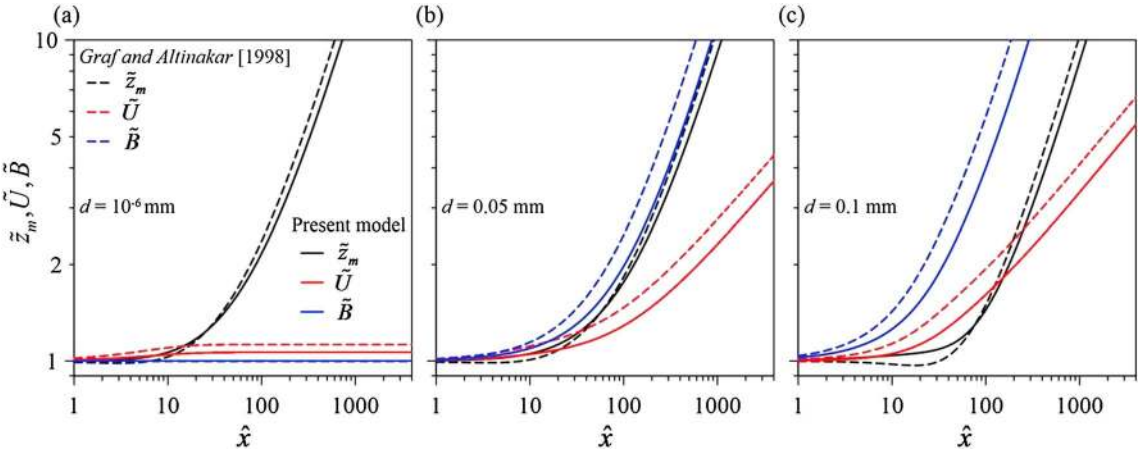

Figure 5. Variations of $\widetilde{z}_m$, $\widetilde{U}$, and $\widetilde{B}$ with $\hat{x}$ in a salinity current with (a) $d = 10^{-6}$ mm, and turbidity currents with (b) $d = 0.05$ mm and (c) $d = 0.1$ mm.

nondimensional reduced sediment flux. In Figures 5–12, the computational results obtained from the present model are shown and compared with those obtained from the formulations (henceforth classical model) of *Graf and Altinakar* [1998].

Figures 5a–5c exhibit the variations of $\widetilde{z}_m$, $\widetilde{U}$, and $\widetilde{B}$ with nondimensional streamwise distance $\hat{x}$ for salinity current with $d = 10^{-6}$ mm and turbidity currents with $d = 0.05$ and 0.1 mm. An increasing trend of $\widetilde{z}_m$ with $\hat{x}$ is evident for all the cases. In Figure 5a, the $\widetilde{U}$ in salinity current increases slowly with $\hat{x}$, becoming invariant of $\hat{x}$ for $\hat{x} > 45$ with a constant value $\widetilde{U} = 1.064$ due to the vanishing acceleration. However, $\widetilde{B}$ is invariant of $\hat{x}$ with a constant value $\widetilde{B} = 1$, since the net sediment flux in salinity current disappears as it is revealed from equation (54). On the contrary, Figures 5b and 5c illustrate the self-accelerating behavior (an increasing trend of $\widetilde{U}$ with $\hat{x}$) for the turbidity currents due to an increasing trend of $\widetilde{B}$ with $\hat{x}$. It is apparent from Figures 5b and 5c that the self-acceleration and the net sediment flux increase with an increase in sediment size in turbidity currents. The $\widetilde{z}_m$ ($\hat{x}$), $\widetilde{U}$ ($\hat{x}$), and $\widetilde{B}$ ($\hat{x}$) curves obtained from the classical formulations [*Graf and Altinakar*, 1998] have similar trends with marginally overestimated results from those obtained from the present model.

It is already stated that the turbidity current is characterized by an erosional or a depositional mode depending on the flow conditions. As the sediment size increases, the nature of turbidity current changes from erosional to depositional mode, primarily due to the effects of the terminal fall velocity of suspended sediment particles. Therefore, for a given bed slope θ, there exists a transition from erosional to depositional mode of turbidity

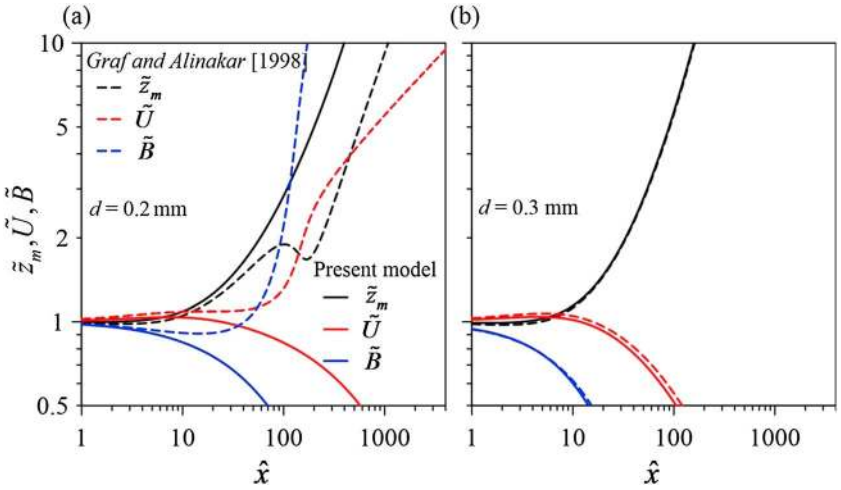

Figure 6. Variations of $\widetilde{z}_m$, $\widetilde{U}$, and $\widetilde{B}$ with $\hat{x}$ in turbidity currents with (a) $d = 0.2$ mm and (b) $d = 0.3$ mm.

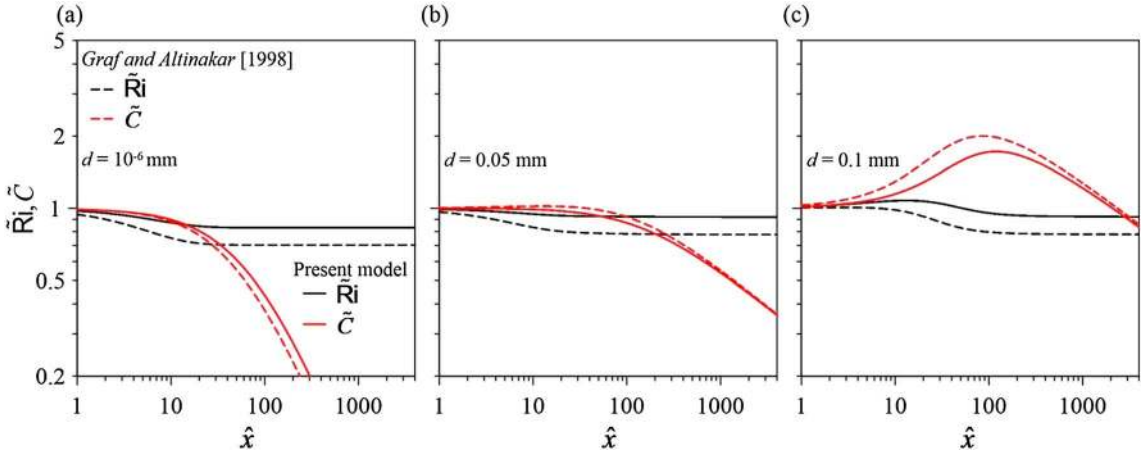

Figure 7. Variations of $\widetilde{\mathrm{Ri}}$ and $\widetilde{C}$ with $\hat{x}$ in a salinity current with (a) $d = 10^{-6}$ mm, and turbidity currents with (b) $d = 0.05$ mm and (c) $d = 0.1$ mm.

currents with an increase in sediment size. To investigate this phenomenon, the variations of $\widetilde{z}_m$, $\tilde{U}$, and $\widetilde{B}$ with $\hat{x}$ for turbidity currents with $d = 0.2$ and 0.3 mm are computed and shown in Figures 6a and 6b. The present model shows a transitional characteristic (erosional to depositional) with an increase in sediment size from $d = 0.1$ to 0.2 mm (see Figures 5c and 6a). However, the classical model of *Graf and Altinakar* [1998] predicts the turbidity current as erosional for $d = 0.2$ mm. On the other hand, Figure 6b shows an agreement between the present and *Graf and Altinakar*'s [1998] models, as the turbidity current is depositional for $d = 0.3$ mm in both the models.

Figures 7a–7c depict the variations of $\widetilde{\mathrm{Ri}}$ and $\widetilde{C}$ with $\hat{x}$ for salinity current with $d = 10^{-6}$ mm and turbidity currents with $d = 0.05$ and 0.1 mm. The $\widetilde{\mathrm{Ri}}$ gradually decreases with $\hat{x}$ in the initial stage, becoming constant (supercritical flow regime) with an increase in $\hat{x}$ for all the cases. In Figure 7a, the $\widetilde{C}$ for salinity current follows a decreasing trend over the entire range of $\hat{x}$, since no sediment is introduced in the current and $\widetilde{z}_m$ continuously increases with $\hat{x}$. In Figure 7b, the $\widetilde{C}$ for turbidity current with $d = 0.05$ mm slowly decreases with $\hat{x}$. On the other hand, in Figure 7c, the $\widetilde{C}$ for turbidity current with $d = 0.1$ mm increases with $\hat{x}$ due to a positive net sediment flux, attaining a maximum value $\widetilde{C} = 1.722$ at $\hat{x} = 120$ and then decreases with $\hat{x}$ even though $\widetilde{B}$ has an increasing trend there (see Figure 5c). The decreasing trend of $\widetilde{C}$ in Figure 7c is attributed to the continuous rapid growth of $\widetilde{z}_m$. The $\widetilde{\mathrm{Ri}}$ ($\hat{x}$) and $\widetilde{C}$ ($\hat{x}$) curves obtained from the classical model [*Graf and Altinakar*, 1998] have similar trends with a slight variation from those obtained from the present study.

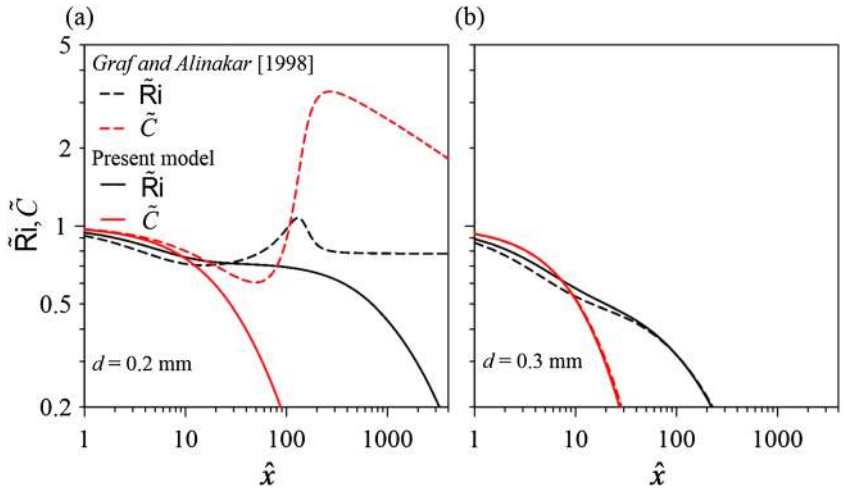

Figure 8. Variations of $\widetilde{\mathrm{Ri}}$ and $\widetilde{C}$ with $\hat{x}$ in turbidity currents with (a) $d = 0.2$ mm and (b) $d = 0.3$ mm.

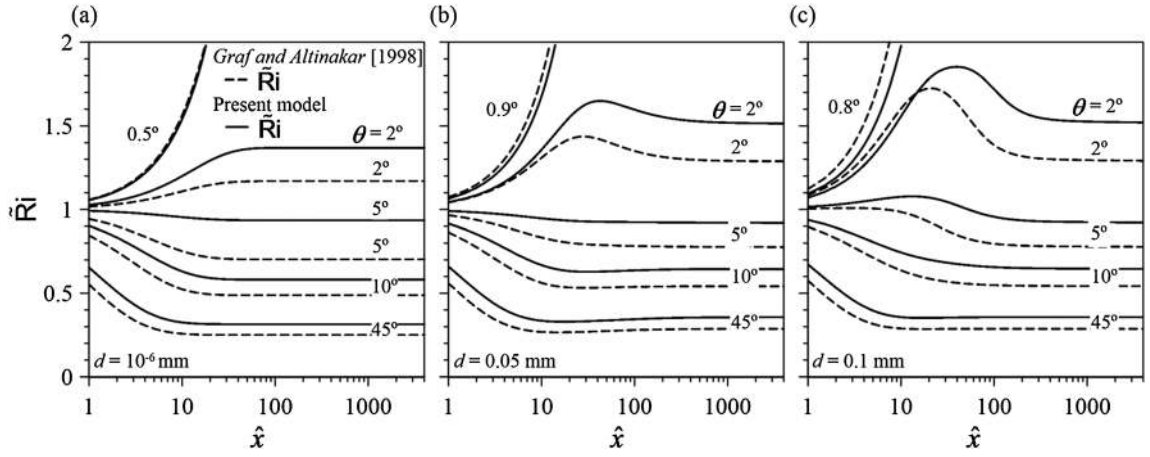

Figure 9. Variations of $\tilde{R}i$ with $\hat{x}$ for different bed slopes θ in a salinity current with (a) $d = 10^{-6}$ mm and turbidity currents with (b) $d = 0.05$ mm and (c) $d = 0.1$ mm.

To demonstrate the transitional characteristic of turbidity currents, the variations of $\tilde{R}i$ and $\tilde{C}$ with $\hat{x}$ for $d = 0.2$ and 0.3 mm are calculated and plotted in Figures 8a and 8b. The transitional characteristic (erosive to depositional) of the turbidity currents is found with an increase in sediment size from $d = 0.1$ to 0.2 mm (see Figures 7c and 8a). However, according to the model of Graf and Altinakar, the turbidity current still shows an erosional mode for $d = 0.2$ mm. On the other hand, for $d = 0.3$ mm, both the models predict the turbidity current as depositional (Figure 8b).

The Richardson number is a good indicator to identify the flow regime (subcritical flow ($Ri > 1$) or supercritical flow ($Ri < 1$)) and, in turn, the turbidity current characteristics (erosional or depositional mode). Figures 9a−9c show the variations of $\tilde{R}i$ with $\hat{x}$ for different θ in salinity current with $d = 10^{-6}$ mm and turbidity currents with $d = 0.05$ and 0.1 mm. It is revealed from Figures 9a to 9c that for smaller values of θ ($\leq 0.8°$), the $\tilde{R}i$ abruptly increases with $\hat{x}$ for all the cases, while for larger values of θ ($\geq 2°$), it increases for $\theta = 2°$ and decreases for $\theta = 5$–45° with $\hat{x}$, becoming invariant of $\hat{x}$ for a large $\hat{x}$. Therefore, to obtain a supercritical flow (independent of $\hat{x}$), it is required to overcome a certain threshold value of bed slope θ that depends on the sediment size. It is evident that the $\tilde{R}i$ in salinity current (Figure 9a) attains a constant value earlier than in turbidity currents (Figures 9b and 9c). The $\tilde{R}i$ ($\hat{x}$) curves obtained from the classical model [*Graf and Altinakar*, 1998] have similar trend with slightly underestimated results from those obtained from the present study for larger values of θ ($\geq 2°$), but slightly overestimated results for smaller values of θ ($\leq 0.8°$).

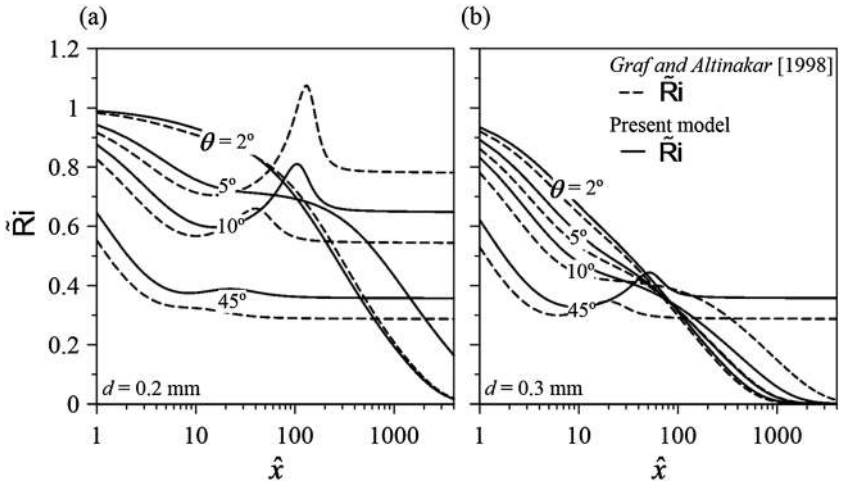

Figure 10. Variations of $\tilde{R}i$ with $\hat{x}$ for different bed slopes θ in turbidity currents with (a) $d = 0.2$ mm and (b) $d = 0.3$ mm.

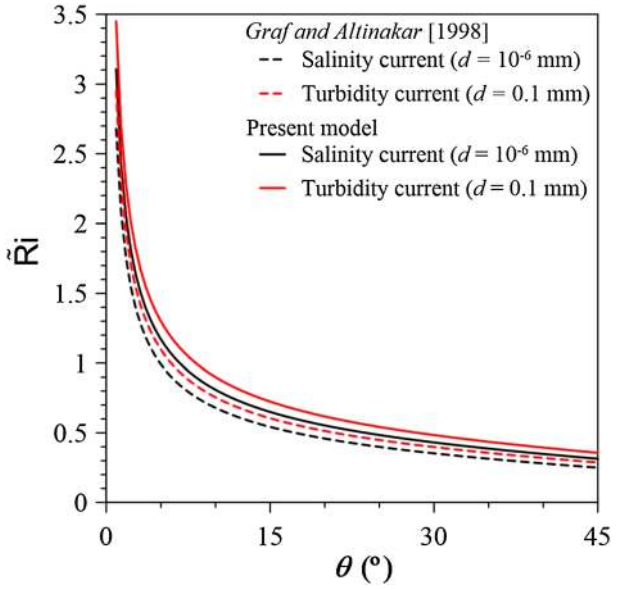

Figure 11. Variations of $\widetilde{\mathrm{Ri}}$ with θ at $\hat{x} = 4000$ in a salinity current with $d = 10^{-6}$ mm and a turbidity current with $d = 0.1$ mm.

Figures 10a and 10b show the variations of $\widetilde{\mathrm{Ri}}$ with $\hat{x}$ for different θ in turbidity currents with $d = 0.2$ and 0.3 mm. In Figure 10a ($d = 0.2$ mm), both the present and *Graf and Altinakar* [1998] models agree well in predicting $\widetilde{\mathrm{Ri}}$ for $\theta = 2°$ but differ for $\theta = 5°$. For $\theta > 5°$, the $\widetilde{\mathrm{Ri}}$ has a supercritical flow tendency (independent of $\hat{x}$), while for $\theta < 5°$, it decays asymptotically toward zero. With an increase in sediment size ($d = 0.3$ mm), the damping of $\widetilde{\mathrm{Ri}}$ is noticeable with θ, while the supercritical flow is achieved at $\theta = 45°$ (Figure 10b). The $\widetilde{\mathrm{Ri}}$ ($\hat{x}$) curves obtained from the classical model [*Graf and Altinakar*, 1998] have similar trend with slightly underestimated results from those obtained from the present study, except for $\theta = 5°$ for which an overestimated result is obtained.

The variations of $\widetilde{\mathrm{Ri}}$ with θ at $\hat{x} = 4000$ (last node of computational domain) for salinity current with $d = 10^{-6}$ mm and turbidity current with $d = 0.1$ mm are plotted in Figure 11. The results obtained from the present model are compared with the formulations of *Graf and Altinakar* [1998]. For a given initial condition, the turbidity currents can only maintain the supercritical flow (Ri < 1) if θ exceeds a threshold value, as shown in Figure 11. The $\widetilde{\mathrm{Ri}}$ (θ) curves obtained from the classical model [*Graf and Altinakar*, 1998] have similar trend with slightly underestimated results from those obtained from the present study.

Figure 12 displays the variations of nondimensional growth rate $d\tilde{z}_m/d\hat{x}$ of turbidity currents with θ at $\hat{x} = 4000$ for salinity current with $d = 10^{-6}$ mm and turbidity current with $d = 0.1$ mm. In these cases, the present model slightly underestimates the growth rate from that obtained from *Graf and Altinakar*'s [1998] model. The ratio of average growth rate of the turbidity current to that of the salinity current is determined as 0.66 (approximately), while from the classical model of *Graf and Altinakar* [1998], this ratio is obtained as 0.67. However, *Akiyama and Stefan* [1985] reported the ratio as 0.65.

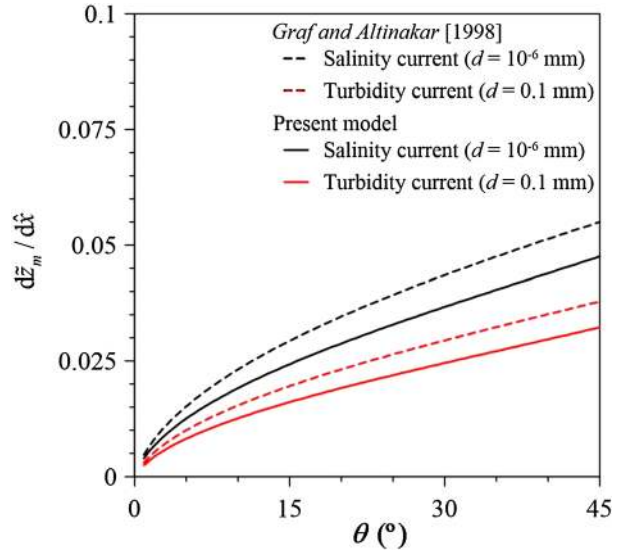

Figure 12. Variations of $d\tilde{z}_m/d\hat{x}$ with θ at $\hat{x} = 4000$ in a salinity current with $d = 10^{-6}$ mm and a turbidity current with $d = 0.1$ mm.

9. Discussion

The present model of turbidity current is not merely based on empirical relationships, but it provides an insight into the physics of the fluid flow. The velocity and concentration distributions reported earlier were typically based on self-similarity functions obtained by treating the depth-averaged variables in the moments of the integral scales. Following the analysis by *Parker et al*. [1986], a satisfactory depth-averaged model was classical model [*Graf and Altinakar*, 1998]. In particular, the knowledge of

the velocity and concentration distributions is required to treat the equations of fluid mass, sediment mass, and fluid momentum balance.

The expression for the velocity distribution is derived in section 3. Using the experimental velocity data of turbidity and salinity currents reported by various investigators, the unknown parameters involved in the velocity distribution function are determined. However, the velocity distributions in a flow over bed forms have a departure from this trend, since the maximum velocity shifts upward in this case [*Sequeiros et al*., 2010]. It is relevant to mention that the generalized expression (equation (11)) for the velocity distribution can also be applicable to the flow over bed forms, if the unknown parameters are adjusted according to the experimental data. Moreover, the unknown parameters involved in the velocity distribution are reduced to a single unknown parameter by means of the boundary conditions and the empirical relations. From the velocity distribution, the flow parameters such as nondimensional depth-averaged velocity, momentum (Boussinesq), and energy (Coriolis) coefficients are determined as 0.52, 1.465, and 2.366, respectively. In contrast, according to *Altinakar et al*. [1996], the nondimensional depth-averaged velocity was found as 0.769 showing a 50% overestimation of the present value. As a result of which the momentum and energy coefficients affect the moments of the integral scales of the governing equations. So they need to be taken into account for a better performance of the model.

The concentration distribution is likewise treated and derived in section 4. Following an analogous derivation to the velocity distribution, a single function for the concentration distribution involving a single unknown parameter is proposed by applying the boundary conditions and the empirical relations. The concentration distribution is based on the near-Gaussian distribution proposed by *Altinakar et al*. [1996] for the outer layer of the turbidity currents. After an appropriate treatment, the near-Gaussian distribution is used over the entire range of the turbidity current layer. So two separate concentration distributions in the inner and outer layers, which make the formulation rather complicated, are no longer required. The experimental data used in the analysis are chosen from the same experiments used for the velocity distribution. Therefore, the level of vanishing velocity at the interface between the turbidity current and the ambient fluid is known, and the ordinate of the concentration distribution is rescaled accordingly. From the viewpoint of the suspended sediment motion, little is known about the background mechanism of the suspended sediment concentration in turbidity currents. Within the inner layer where the velocity distribution follows a classical boundary layer flow, the concentration distribution is expected to adopt a traditional concentration distribution, as proposed by *Rouse* [1937]. However, according to the experimental data trend, the concentration at the bed can be approximated with a finite value [*Altinakar et al*., 1996]. Within the outer layer, the concentration distribution has a decreasing trend with the vertical distance leaving a finite value at the interface between the turbidity current and the ambient fluid. Accordingly, the moments of the integral scales defined in equation (5) are performed neglecting the concentration distribution in the ambient fluid layer.

Using the velocity and concentration distributions, the characteristics of turbidity current are further analyzed. In section 5, the turbulent diffusivity in turbidity currents is estimated using the diffusion equation of the suspended sediment concentration. The Reynolds shear stress in turbidity currents is computed applying the Boussinesq hypothesis. The Reynolds shear stress distribution is in agreement with the theoretical study reported by *Stacey and Bowen* [1988]. Applying the diffusion equation to the suspended sediment motion, the turbulent diffusivity distribution is also obtained. In contrast to the present observations, the study of *Stacey and Bowen* [1988] considered a linear bridge to join the bimodal type of turbulent diffusivity distribution following *Launder and Spalding* [1972]. This linear bridge was explained from the viewpoint of the Prandtl's mixing length theory for turbidity currents. In fact, nothing can be firmly stated in this aspect, since little is known about the characteristics of the turbulent length scales in turbidity currents. However, the present study is free from the consideration of a linear bridge.

The present model provides the gradually varied flow formulations given in section 6. The variations of the nondimensional turbidity current depth, velocity, concentration, reduced sediment flux, and Richardson number with nondimensional streamwise distance obtained from the present model are compared with those obtained from the classical model [*Graf and Altinakar*, 1998]. The variations of $\widetilde{z}_m$, $\widetilde{U}$, $\widetilde{C}$, and $\widetilde{B}$ are, in general, underestimated by the present model as compared to those obtained from the classical model, leading to milder transitions than in the classical model. The variation of $\widetilde{\mathrm{Ri}}$ is, in contrast, overestimated. Consequently, it can be interpreted that the present model is able to describe a greater strength of erosional

turbidity currents without the implication of greater values of $\widetilde{z}_m$, $\widetilde{U}$, $\widetilde{C}$, and $\widetilde{B}$. Additionally, the point of departure from the erosional to depositional turbidity current appears earlier in the present model than in the classical model with respect to the median size of sediment particles, as inferred from Figures 6 and 8. The reason is attributed to account for the self-preserving type distributions of velocity and concentration in the present model. It is one of the main differences between the present and the classical models. Besides, the difference in prediction of $\widetilde{\mathrm{Ri}}$ for different bed slopes θ is analyzed in Figure 11. In addition, the same trend is found for the growth rate $\mathrm{d}\widetilde{z}_m/\mathrm{d}x$ of turbidity currents in Figure 12 by analyzing the ratio of the growth rates in salinity to turbidity currents. These characteristics are generalized for a wide range of θ, and in turn, it can be stated that the present model in general performs similarly to the classical model.

Last but not the least, the results on the gradually varied flow parametric variables in turbidity currents with erosional or depositional mode could not be compared with the observed data due to lack of experimental or field data. However, in spite of some approximations adopted in the analysis, this model, at least, fulfills the purpose of describing clearly the characteristics and the behavior of turbidity currents. This corollary is further discussed in Appendix C through an auxiliary calculation following the recommendation of *Parker et al*. [1986]. The present three-equation model does not fail in predicting turbidity currents from ignition point and, in turn, does not violate the four-equation TKE balance [*Hu et al*., 2015]. Besides, in view of the self-preserving type of velocity and concentration laws that are validated by the experimental data and used to develop the gradually varied flow relationships, perhaps a more than a qualitative rationality can be claimed for the computed results.

10. Conclusions

A physically based hydrodynamic analysis for the turbidity currents over a plane bed is presented using the classical three-equation model (depth-averaged fluid continuity, sediment continuity, and fluid momentum equations) and considering the self-similar characteristics of the streamwise velocity and concentration distributions. According to the classical theory of sediment-laden flow, the governing equations of turbidity currents are presented in generalized forms by using the moments of the integral scales. To perform the integrals, the velocity and concentration distributions are assumed as single functions over the entire turbidity current layer. Using the experimental data of salinity and turbidity currents over plane beds, the unknown parameters involved in the velocity and concentration distributions are evaluated. Importantly, the velocity and concentration distributions are of self-preserving type, as they correspond closely to the wide range of experimental data in fully developed flows. The values of the typical flow parameters, such as depth-averaged velocity, momentum, and energy coefficients, are evaluated from the velocity distribution. From the velocity and concentration distributions, the turbulent diffusivity and the Reynolds shear stress distributions are determined using the diffusion equation of suspended sediment concentration and the Boussinesq hypothesis. The turbulent diffusivity distribution is found to follow a different trend to that reported in the literature [*Stacey and Bowen*, 1988], while the Reynolds shear stress distribution agrees well with the previous observations [*Dey et al*., 2010].

Using the velocity and concentration distributions in the moments of the integral scales, a generalized model for unsteady nonuniform turbidity currents is developed. Then, the gradually varied flow formulations for steady nonuniform turbidity currents are derived from the generalized model with suitable closure relationships. The different parametric variables (current depth, velocity, concentration, reduced sediment flux, and Richardson number) of turbidity currents obtained from the present model are compared with those obtained from the model of *Graf and Altinakar* [1998]. The dependency of the parametric variables of turbidity currents on the sediment size and the bed slope including the transitional feature of turbidity currents from erosional to depositional mode is especially focused. The threshold value (erosional to depositional mode) of the streamwise bed slope that ensures a supercritical flow is highlighted for different sediment sizes. However, for depositional turbidity currents carrying larger sediment sizes, no threshold value of the bed slope is obtained. The ratio of growth rate of the turbidity current to that of the salinity current predicted by the present model is found almost similar to those obtained from previous models.

The limitations of this study are as follows:

1. The expressions for self-preserving distributions of velocity and concentration are calibrated using the limited available experimental data reported by some investigators. Use of more experimental data could improve the accuracy of these expressions.

2. The diffusion equation of suspended sediment concentration for uniform flow is applied for solving the gradually varied turbidity current equations. Thus, the turbidity current is assumed to be a pseudouniform flow.
3. The suspended sediment concentration is assumed to be sufficiently small to apply the Boussinesq approximation, and thus, the kinematic viscosity equals its value for clear water.
4. The present study does not take into account the effects of bed forms on turbidity current over sediment beds.

Nevertheless, the present model is believed to be a powerful tool to analyze the characteristics of fully developed turbidity currents. It not only provides more comprehensive insights into the vertical structure of the currents but also the generalized formulation of unsteady nonuniform turbidity currents and parametric variations of gradually varied turbidity currents. In addition, it provides additional evidences to claim in favor of the three-equation model.

Appendix A: TKE Budget

The depth-averaged equation of TKE budget of turbidity currents is as follows [*Parker et al.*, 1986]:

$$\frac{\partial}{\partial t}\int_0^\infty k\mathrm{d}z+\frac{\partial}{\partial x}\int_0^\infty uk\mathrm{d}z=P_T-\int_0^\infty \varepsilon \mathrm{d}z-\frac{1}{2}\Delta_s g w_s\int_0^\infty c\mathrm{d}z \\ -\Delta_s g\left[\frac{\partial}{\partial t}\int_0^\infty\int_z^\infty c\mathrm{d}z\mathrm{d}z+\frac{\partial}{\partial x}\int_0^\infty\int_z^\infty uc\mathrm{d}z\mathrm{d}z+\int_0^\infty c\frac{\partial}{\partial x}\left(\int_0^z u\mathrm{d}z\right)\mathrm{d}z\right]\cos\theta, \tag{A1}$$

where k is the TKE, P_T is the average TKE production rate, and ε is the TKE dissipation rate.

The link of equation (A1) with the three-equation model was expressed by *Parker et al.* [1986] through the bed shear stress. The entrainment coefficient, $E_s = E_b/w_s$, is related to the state of the turbulence, as it can be inferred from equation (7) and is given as a function of the level of turbulence K, which is the depth-averaged TKE. Thereby, *Parker et al.* [1986] assumed

$$u_{*_b}^2=\alpha_1 K, \tag{A2}$$

where α_1 is the proportionality parameter, which is assumed to be constant for a given flow. In addition, following *Parker et al.* [1986], one can write

$$\varepsilon_0 z_m=\int_0^\infty \varepsilon\mathrm{d}z=U^3\left[\frac{1}{2}E_w\left(1-\mathrm{Ri}-2\frac{K}{U^2}\right)+\alpha_1\frac{K}{U^2}\right] \quad \text{and} \tag{A3}$$

$$P_T=Pz_m. \tag{A4}$$

The integrals of equation (A1) are defined as

$$I_6=\int_0^\infty\int_z^\infty uc\mathrm{d}z\mathrm{d}z,\ I_7=\int_0^\infty c\frac{\partial}{\partial x}\left(\int_0^z u\mathrm{d}z\right)\mathrm{d}z,\ I_8=\int_0^\infty k\mathrm{d}z, \quad \text{and} \quad I_9=\int_0^\infty uk\mathrm{d}z. \tag{A5}$$

Then, the generalized form of equation (A1) is given by

$$\frac{\partial I_8}{\partial t}+\frac{\partial I_9}{\partial x}=(P-\varepsilon_0)z_m-\frac{1}{2}\Delta_s g w_s I_3-\Delta_s g\left(\frac{\partial I_5}{\partial t}+\frac{\partial I_6}{\partial x}+I_7\right)\cos\theta. \tag{A6}$$

Including equation (A1) in the turbidity current model, the large values of E_s damp the turbulence state and hence stabilizes the values of K and E_s, which is unpredictable by a three-equation model [*Parker et al.*, 1986]. However, in order to obtain a solution for equation (A6), additional information is required. The TKE distribution belongs to integrals I_8 and I_9. Unfortunately, little is known about the legitimate TKE distribution in turbidity currents. Although there exist some approximations of the TKE distribution in turbidity currents [*Islam and Imran*, 2010], they are not generalized. Besides not only the expression for TKE distribution is required in a complete four-equation model but also an initial value of TKE is a prerequisite to initiate the computation. In fact, it was clearly pointed out by *Parker et al.* [1986] that the initial value of TKE for the computation requires a number of assumptions. Therefore, it is rather uncertain to provide a reliable

initial value of TKE. In addition, the type of distributions assumed for the velocity, and the concentration makes it difficult to perform the other integral scales. In fact, integral I_7 is not possible to be integrated in terms of a function of z, as the hypergeometric series functions appear, e.g., Kummer confluent hypergeometric functions. Also, in order to perform the integration of I_6, a similar continuous function is assumed for the product of the nondimensional velocity and concentration as $\hat{u}\hat{c} = 10.5\eta^{0.75}(1-\eta)^5$. Thereby, I_6 is

$$I_6 = \int_0^{\infty}\int_z^{\infty} u c \mathrm{d}z\mathrm{d}z = \int_0^{z_m}\int_z^{z_m} u c \mathrm{d}z\mathrm{d}z \simeq 10.5 U_m C_m z_m^2 \int_0^1\int_\eta^1 \eta^{0.75}(1-\eta)^5 \mathrm{d}\eta\mathrm{d}\eta = 0.086\, U_m C_m z_m^2. \tag{A7}$$

Thus, equation (A1) is finally modified as

$$\frac{\partial I_8}{\partial t} + \frac{\partial I_9}{\partial x} = (P-\varepsilon_0) z_m - \Delta_s g \left\{ 0.264\, w_s C_m z_m - \left[0.134 \frac{\partial \left(C_m z_m^2\right)}{\partial t} + 0.086 \frac{\partial \left(U_m C_m z_m^2\right)}{\partial x} + I_7 \right] \cos\theta \right\}. \tag{A8}$$

The consideration of equation (A8) may enhance the performance of the turbidity current model [*Parker et al.*, 1986]. Notwithstanding, realizing the drawbacks, the inclusion of this equation can be avoided by adopting proper closure relationships in three-equation model.

Appendix B: The Moments of the Integral Scales

With the unknown parameters, the velocity and concentration distributions obtained from equations (16) and (31) are given as

$$\hat{u} = 4.284\,\eta^{0.6}(1-\eta)^{2.2} \quad \text{and} \tag{B1}$$

$$\hat{c} = 1.486 \exp\left(-4\eta^{1.5}\right). \tag{B2}$$

Therefore, the moments of the integral scales are

$$I_1 = \int_0^{\infty} u \mathrm{d}z = \int_0^{z_m} u \mathrm{d}z = U_m z_m \int_0^1 \hat{u}\mathrm{d}\eta = 4.284\, U_m z_m \int_0^1 \eta^{0.6}(1-\eta)^{2.2}\mathrm{d}\eta = 0.52\, U_m z_m, \tag{B3}$$

$$I_2 = \int_0^{\infty} u^2 \mathrm{d}z = \int_0^{z_m} u^2 \mathrm{d}z = U_m^2 z_m \int_0^1 \hat{u}^2 \mathrm{d}\eta = 18.35\, U_m^2 z_m \int_0^1 \eta^{1.2}(1-\eta)^{4.4}\mathrm{d}\eta = 0.396\, U_m^2 z_m, \tag{B4}$$

$$I_3 = \int_0^{\infty} c \mathrm{d}z = \int_0^{z_m} c \mathrm{d}z = C_m z_m \int_0^1 \hat{c}\mathrm{d}\eta = 1.486\, C_m z_m \int_0^1 \exp\left(-4\eta^{1.5}\right)\mathrm{d}\eta = 0.528\, C_m z_m, \tag{B5}$$

$$\begin{aligned} I_4 &= \int_0^{\infty} u c \mathrm{d}z = \int_0^{z_m} u c \mathrm{d}z = U_m C_m z_m \int_0^1 \hat{u}\hat{c}\mathrm{d}\eta \\ &= 6.365\, U_m C_m z_m \int_0^1 \exp\left(-4\eta^{1.5}\right)\eta^{0.6}(1-\eta)^{2.2}\mathrm{d}\eta = 0.396\, U_m C_m z_m \quad \text{and} \end{aligned} \tag{B6}$$

$$\begin{aligned} I_5 &= \int_0^{\infty}\int_z^{\infty} c \mathrm{d}z\mathrm{d}z = \int_0^{z_m}\int_z^{z_m} c \mathrm{d}z\mathrm{d}z = C_m z_m^2 \int_0^1\int_\eta^1 \hat{c}\mathrm{d}\eta\mathrm{d}\eta \\ &= 1.486\, C_m z_m^2 \int_\eta^1\int_\eta^1 \exp\left(-4\eta^{1.5}\right)\mathrm{d}\eta\mathrm{d}\eta = 0.743\, C_m z_m^2. \end{aligned} \tag{B7}$$

Appendix C: A Comparison Between Three-Equation and Classical Four-Equation Models

According to *Parker et al.* [1986], the self-accelerating currents are wrongly predicted by means of the former classical three-equation models [*Ellison and Turner*, 1959]. On the contrary, they are satisfactorily simulated

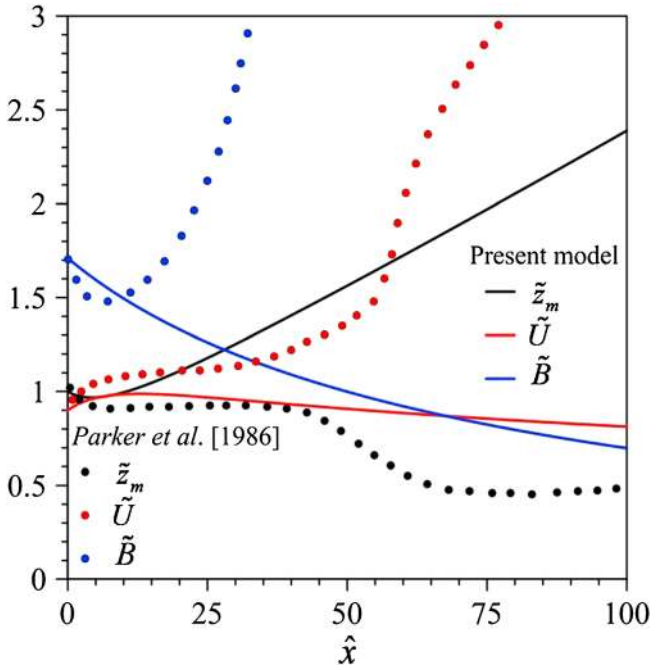

Figure C1. Variations of $\widetilde{z}_m$, $\widetilde{U}$, and $\widetilde{B}$ with $\hat{x}$ in a turbidity current showing the comparison between the present model and *Parker et al.* [1986].

by introducing the TKE budget equation in the model. In this regard, Figure 7b from *Parker et al.* [1986] are taken and replotted (see Figures C1 and C2, respectively) to assess the performance of the three-equation model of this study. Figure C1 shows the development of the turbidity current characteristics from *ignition*. The term ignition in turbidity current is defined by *Parker et al.* [1986] as the self-acceleration through an entrainment of bed sediment. The curve illustrates how the three-equation model of *Parker et al.* [1986] fails to represent the behavior of the current. However, the three-equation model of this study does not describe such a rapid increase in the sediment transport as obtained by *Parker et al.* [1986]. In addition, Figure C2 depicts how the present model corresponds to the estimations by four-equation model of *Parker et al.* [1986] rather than to follow the hydraulic jump trend obtained from the classical three-equation model of *Parker et al.* [1986].

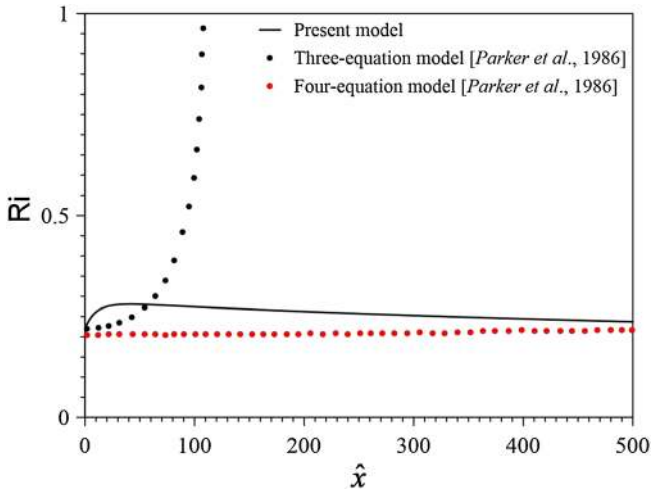

Figure C2. Variation of Ri with $\hat{x}$ in a turbidity current showing the comparison between the present model and *Parker et al.* [1986].

Notation

B	reduced sediment flux
$\widetilde{B}$	nondimensional reduced sediment flux ($= B/B_0$)
B_0	initial condition of B
C	depth-averaged concentration
$\hat{C}$	C/C_m
$\widetilde{C}$	nondimensional depth-averaged concentration ($= C/C_0$)
C_0	initial condition of C
C_m	suspended sediment concentration at $\eta = \eta_w$
c	suspended sediment concentration in turbidity current at z
c'	fluctuations of c
$\hat{c}$	c/C_m
c_0	sediment concentration at bed
$\hat{c}_0$	c_0/C_m
c_b	reference sediment concentration
$\overline{c'w'}$	Reynolds flux of suspended sediment particles
D_b	deposition rate of sediment
d	median size of sediment particles
E_b	erosion rate of sediment
E_s	entrainment coefficient of sediment particles from bed
E_w	entrainment coefficient of ambient fluid
g	gravitational acceleration
I_{1-8}	moments of integral scales
K	level of turbulence
k	turbulent kinetic energy (TKE)
P_T	average TKE production rate
Re_p	particle Reynolds number [$= (\Delta_s g d^3/\upsilon^2)^{0.5}$]
Ri	Richardson number
$\widetilde{\mathrm{Ri}}$	relative Richardson number ($= \mathrm{Ri}/\mathrm{Ri}_0$)
Ri_0	initial condition of Ri
t	time
U	depth-averaged velocity
$\hat{U}$	U/U_m
$\widetilde{U}$	nondimensional depth-averaged velocity ($= U/U_0$)
U_0	initial condition of U
U_m	maximum velocity
u	streamwise velocity of turbidity current at z
$\hat{u}$	u/U_m
u_{*b}	shear velocity
w	vertical velocity component
w'	fluctuations of w
w_h	vertical velocity component at top of turbidity current
w_s	terminal fall velocity of suspended sediment particles
x, z	Cartesian coordinates
$\hat{x}$	x/z_{m0}
Z	Rouse number [$= w_s/(\kappa u_{*b})$]
z_m	turbidity current depth
$\widetilde{z}_m$	nondimensional turbidity current depth ($= z/z_{m0}$)
z_{m0}	initial condition of z_m
z_w	position of maximum velocity
α	energy (Coriolis) coefficient
β	momentum (Boussinesq) coefficient
χ, ξ	exponents in velocity distribution

Δ_s	submerged relative density
ε	TKE dissipation rate
ε_0	layer averaged TKE dissipation rate
ε_t	turbulent diffusivity
$\hat{\varepsilon}_t$	$\varepsilon_t/(ku_{*b}z_m)$
$\Gamma(s)$	Euler gamma function
$\Gamma(a, s)$	incomplete gamma function
η	z/z_m
η_w	z_w/z_m
κ	von Kármán constant
λ, ϕ, ζ	unknown parameters in concentration distribution
λ_D	Darcy-Weisbach friction factor
θ	streamwise bed slope
ρ	mass density of fluid-sediment mixture $[=\rho_a+(\rho_s-\rho_a)c]$
ρ_a	mass density of ambient fluid
ρ_s	mass density of sediment particles
σ	coefficient
τ	Reynolds shear stress
$\hat{\tau}$	$\tau/(\rho u_{*_b}^2)$
$\widetilde{\tau}$	$\hat{\tau}\ (u_{*b}/U_m)$
υ	kinematic viscosity of fluid

Acknowledgments

This study was supported by the Spanish project CTM2013-45666-R, Ministerio de Economía y Competitividad. The first author is thankful to the Ministerio de Educación, Cultura y Deporte, Spain, for grant (FPU12/04795) to visit to the Indian Institute of Technology (IIT) Kharagpur. Data supporting Figures 2 and 3 are available in *Parker et al.* [1987], *García* [1993], *Altinakar et al.* [1996], *Islam and Imran* [2010], *Sequeiros et al.* [2010], and *Nourmohammadi et al.* [2011], as also acknowledged in the corresponding figure legends.

References

Ahrens, J. P. (2000), A fall-velocity equation, *J. Waterw. Port Coastal Ocean Eng.*, *126*(2), 99–102.

Akiyama, J., and H. Stefan (1985), Turbidity current with erosion and deposition, *J. Hydraul. Eng.*, *111*(12), 1473–1496, doi:10.1061/(ASCE)0733-9429(1985)111:12(1473).

Altinakar, M. S., W. H. Graf, and E. J. Hopfinger (1993), Water and sediment entrainment in weakly depositing turbidity currents on small slopes in *Proceedings of the 5th Congress*, vol. 2, Int. Assoc. Hydraul. Res., Tokyo, Japan.

Altinakar, M. S., W. H. Graf, and E. J. Hopfinger (1996), Flow structure in turbidity currents, *J. Hydraul. Res.*, *34*(5), 713–718, doi:10.1080/00221689609498467.

Ashida, K., and S. Egashira (1975), Basic study on turbidity currents, *Trans. Jpn. Soc. Civ. Eng.*, *237*, 37–50.

Bagnold, R. A. (1962), Auto-suspension of transported sediment; turbidity currents, *Proc. R. Soc. London, Ser. A*, *265*(1322), 315–319.

Bonnefille, R., and J. Goddet (1959), Etude des courants de densité en canal, in *Proceedings of the 8th Congress*, vol. 2, Int. Assoc. Hydraul. Res., Montreal, Canada.

Chang, H. K., and J. C. Liou (2001), Discussion of 'The fall-velocity equation', *J. Waterw. Port Coastal Ocean Eng.*, *127*(4), 250–251.

Dey, S. (2014), *Fluvial Hydrodynamics: Hydrodynamic and Sediment Transport Phenomena*, Springer, Berlin.

Dey, S., T. K. Nath, and S. K. Bose (2010), Submerged wall jets subjected to injection and suction from the wall, *J. Fluid Mech.*, *653*, 57–97, doi:10.1017/S0022112010000182.

Dietrich, W. E. (1982), Settling velocity of natural particles, *Water Resour. Res.*, *18*(6), 1615–1626, doi:10.1029/WR018i006p01615.

Dutta, S., C. Pantano-Rubino, M. I. Cantaero, M. H. Garcia, and G. Parker (2012), Effects of self-stratification on turbidity currents: A large eddy simulation approach, in *Proceedings of the XIX International Conference on Water Resources*, pp. 1–10, Univ. of Illinois at Urbana-Champaign.

Ellison, T. H., and J. S. Turner (1959), Turbulent entrainment in stratified flows, *J. Fluid Mech.*, *6*(3), 423–448, doi:10.1017/S0022112059000738.

Felix, M. (2001), A two-dimensional numerical model for a turbidity current, in *Particulate Gravity Currents*, *Spec. Publ. Int. Assoc. Sedimentol.*, vol. 31, edited by W. McCaffrey, B. Kneller, and J. Peakall, pp. 71–81, Blackwell Ltd., Oxford, U. K.

Fukushima, Y., G. Parker, and H. M. Pantin (1985), Prediction of ignitive turbidity currents in Scripps submarine canyon, *Mar. Geol.*, *67*(1–2), 55–81, doi:10.1016/0025-3227(85)90148-3.

García, M. H. (1993), Hydraulic jumps in sediment-driven bottom currents, *J. Hydraul. Eng.*, *119*(10), 1094–1117, doi:10.1061/(ASCE)0733-9429(1993)119:10(1094).

Graf, W. H. (1971), *Hydraulics of Sediment Transport*, McGraw-Hill, New York.

Graf, W. H., and M. S. Altinakar (1998), *Fluvial Hydraulics*, John Wiley, New York.

Guo, J. (2002), Logarithmic matching and its applications in computational hydraulics and sediment transport, *J. Hydraul. Res.*, *40*(5), 555–565, doi:10.1080/00221680209499900.

Hallermeier, R. J. (1981), Terminal settling velocity of commonly occurring sand grains, *Sedimentology*, *28*(6), 859–865, doi:10.1111/j.1365-3091.1981.tb01948.x.

Hu, P., Z. Cao, G. Pender, and G. Tan (2012), Numerical modelling of turbidity currents in the Xiaolangdi reservoir, Yellow River, China, *J. Hydrol.*, *464–465*, 41–53, doi:10.1016/j.jhydrol.2012.06.032.

Hu, P., T. Pähtz, and Z. He (2015), Is it appropriate to model turbidity currents with the three-equation model?, *J. Geophys. Res. Earth Surf.*, *120*, 1153–1170, doi:10.1002/2015JF003474.

Inman, D. L., C. E. Nordstrom, and R. E. Flick (1976), Currents in submarine canyons: An air-sea-land interaction, *Annu. Rev. Fluid Mech.*, *8*, 275–310, doi:10.1146/annurev.fl.08.010176.001423.

Islam, M. A., and J. Imran (2010), Vertical structure of continuous release saline and turbidity currents, *J. Geophys. Res.*, *115*, C08025, doi:10.1029/2009JC005365.

Lai, Y., J. Huang, and K. Wu (2015), Reservoir turbidity current modeling with a two-dimensional layer-averaged model, *J. Hydraul. Eng.*, 04015029, doi:10.1061/(ASCE)HY.1943-7900.0001041.
Launder, B. E., and D. B. Spalding (1972), *Mathematical Models of Turbulence*, Academic press, New York.
Lizhong, Y., Y. Junqi, and W. Yafei (2011), Simulation of gravity currents using the thermal lattice Boltzmann method, *Int. J. Numer. Meth. Fluids*, *66*(9), 1174–1182, doi:10.1002/fld.2308.
Mahdinia, M., B. Firoozabadi, M. Farshchi, A. G. Varnamkhasti, and H. Afshin (2011), Large eddy simulation of lock-exchange flow in a curved channel, *J. Hydraul. Eng.*, *138*(1), 57–70, doi:10.1061/(ASCE)HY.1943-7900.0000482.
Mastbergen, D. R., and J. H. Van Den Berg (2003), Breaching in fine sands and the generation of sustained turbidity currents in submarine canyons, *Sedimentology*, *50*(4), 625–637, doi:10.1046/j.1365-3091.2003.00554.x.
Normark, W. R., and F. H. Dickson (1976), Man-made turbidity currents in Lake Superior, *Sedimentology*, *23*(6), 815–831, doi:10.1111/j.1365-3091.1976.tb00110.x.
Nourmohammadi, Z., H. Afshin, and B. Firoozabadi (2011), Experimental observation of the flow structure of turbidity currents, *J. Hydraul. Res.*, *49*(2), 168–177, doi:10.1080/00221686.2010.543777.
Parker, G., Y. Fukushima, and H. M. Pantin (1986), Self-accelerating turbidity currents, *J. Fluid Mech.*, *171*, 145–181, doi:10.1017/S0022112086001404.
Parker, G., M. H. Garcia, Y. Fukushima, and W. Yu (1987), Experiments on turbidity currents over an erodible bed, *J. Hydraul. Res.*, *25*(1), 123–147, doi:10.1080/00221688709499292.
Piper, D. J. W., P. Cochonat, and M. L. Morrison (1999), The sequence of events around the epicentre of the 1929 Grand Banks earthquake: Initiation of debris flows and turbidity current inferred from sidescan sonar, *Sedimentology*, *46*(1), 79–97, doi:10.1046/j.1365-3091.1999.00204.x.
Pratson, L. F., J. Imran, G. Parker, J. P. M. Syvitski, and E. Hutton (2000), Debris flows vs. turbidity currents: a modeling comparison of their dynamics and deposits, in *Fine-Grained Turbidite Systems*, *Am. Assoc. Petrol. Geol. Mem. 72, Spec. Publ.*, vol. 68, edited by A. H. Bouma and C. G. Stone, pp. 57–71, Soc. for Sediment. Geol., Tulsa, Okla.
Prestininzi, P., G. Sciortino, and M. L. Rocca (2013), On the effect of the intrinsic viscosity in a two-layer shallow water lattice Boltzmann model of axisymmetric density currents, *J. Hydraul. Res.*, *51*(6), 668–680, doi:10.1080/00221686.2013.819532.
Rouse, H. (1937), Modern conceptions of the mechanics of turbulence, *Trans. Am. Soc. Civ. Eng.*, *102*(1), 463–505.
Sequeiros, O. E., B. Spinewine, R. T. Beaubouef, T. Sun, M. H. García, and G. Parker (2010), Characteristics of velocity and excess density profiles of saline underflows and turbidity currents flowing over a mobile bed, *J. Hydraul. Eng.*, *136*(7), 412–433, doi:10.1061/(ASCE)HY.1943-7900.0000200.
Shringarpure, M., M. I. Cantero, and S. Balachandar (2012), Dynamics of complete turbulence suppression in turbidity currents driven by monodisperse suspensions of sediment, *J. Fluid Mech.*, *712*, 384–417, doi:10.1017/jfm.2012.427.
Stacey, M. W., and A. J. Bowen (1988), The vertical structure of density and turbidity currents: Theory and observations, *J. Geophys. Res.*, *93*(C4), 3528–3542, doi:10.1029/JC093iC04p03528.
Stefan, H. (1973), High concentration turbidity currents in reservoirs in *Proceedings of the 15th Congress*, pp. 341–352, Int. Assoc. Hydraul. Res., Istanbul, Turkey.
Sumner, E. J., and C. K. Paull (2014), Swept away by a turbidity current in Mendocino submarine canyon, California, *Geophys. Res. Lett.*, *41*, 7611–7618, doi:10.1002/2014GL061863.
Turner, J. S. (1973), *Buoyancy Effects in Fluids*, Cambridge Univ. Press, Great Britain.
Wang, H., N. Bi, Y. Saito, Y. Wang, X. Sun, J. Zhang, and Z. Yang (2010), Recent changes in sediment delivery by the Huanghe (Yellow River) to the sea: Causes and environmental implications in its estuary, *J. Hydrol.*, *391*(3–4), 302–313, doi:10.1016/j.jhydrol.2010.07.030.
Wu, W. (2008), *Computational River Dynamics*, Taylor and Francis, London.
Wu, W., and S. S. Y. Wang (2006), Formulas for sediment porosity and settling velocity, *J. Hydraul. Eng.*, *132*(8), 858–862, doi:10.1061/(ASCE)0733-9429(2006)132:8(858).
Zhang, R. J., and J. H. Xie (1993), *Sedimentation Research in China: Systematic Selections*, China Water and Power Press, Beijing.